

The host galaxies of luminous type 2 AGN at $z \sim 0.3-0.4$

J.J. Urbano-Mayorgas^{1*}, M. Villar Martín¹, F. Buitrago², J. Piqueras López¹

B. Rodríguez del Pino¹, A. M. Koekemoer³, M. Huertas-Company^{4,5}

R. Domínguez-Tenreiro^{6,7}, F.J. Carrera⁸, C. Tadhunter⁹

¹Centro de Astrobiología (CSIC-INTA), Carretera de Ajalvir, km 4, 28850 Torrejón de Ardoz, Madrid, Spain

²Instituto de Astrofísica e Ciências do Espaço, Universidade do Lisboa, Tapada da Ajuda - Edifício Leste 2 Piso, 1349-018, Lisboa, Portugal

³Space Telescope Science Institute, 3700 San Martin Drive, Baltimore, MD 21218, USA

⁴Sorbonne Université, Observatoire de Paris, Université PSL, CNRS, LERMA, F-75014, Paris, France

⁵Sorbonne Paris Cité, Université Paris Diderot, 5 Rue Thomas Mann, F-75013, France

⁶Dept. de Física Teórica, Univ. Autónoma de Madrid, E-28049 Cantoblanco Madrid, Spain

⁷Astro-UAM, UAM, Unidad Asociada CSIC, E-28049 Cantoblanco, Madrid, Spain

⁸Instituto de Física de Cantabria (CSIC-UC), Avenida de los Castros, E-39005 Santander, Spain

⁹Department of Physics and Astronomy, University of Sheffield, Sheffield S3 7RH, UK

Accepted ?. Received ?; in original form ?.

ABSTRACT

We study the morphological and structural properties of the host galaxies associated with 57 optically-selected luminous type 2 AGN at $z \sim 0.3-0.4$: 16 high-luminosity Seyfert 2 (HLSy2, $8.0 \leq \log(L_{[\text{OIII}]} / L_{\odot}) < 8.3$) and 41 obscured quasars (QSO2, $\log(L_{[\text{OIII}]} / L_{\odot}) \geq 8.3$). With this work, the total number of QSO2 at $z < 1$ with parametrized galaxies increases from ~ 35 to 76. Our analysis is based on HST WFPC2 and ACS images that we fit with GALFIT. HLSy2 and QSO2 show a wide diversity of galaxy hosts. The main difference lies in the higher incidence of highly-disturbed systems among QSO2. This is consistent with a scenario in which galaxy interactions are the dominant mechanism triggering nuclear activity at the highest AGN power. There is a strong dependence of galaxy properties with AGN power (assuming $L_{[\text{OIII}]}$ is an adequate proxy). The relative contribution of the spheroidal component to the total galaxy light (B/T) increases with $L_{[\text{OIII}]}$. While systems dominated by the spheroidal component spread across the total range of $L_{[\text{OIII}]}$, most disk-dominated galaxies concentrate at $\log(L_{[\text{OIII}]} / L_{\odot}) < 8.6$. This is expected if more powerful AGN are powered by more massive black holes which are hosted by more massive bulges or spheroids. The average galaxy sizes ($\langle r_e \rangle$) are 5.0 ± 1.5 kpc for HLSy2 and 3.9 ± 0.6 kpc for HLSy2 and QSO2 respectively. These are significantly smaller than those found for QSO1 and narrow line radio galaxies at similar z . We put the results of our work in context of related studies of AGN with quasar-like luminosities.

Key words:

galaxies: active - galaxies: evolution - galaxies:quasars:general

1 INTRODUCTION

Studies of the host galaxies associated with active galactic nuclei (AGN) are relevant on a diversity of topics related to galaxy formation and evolution such as: What mechanisms control nuclear activity and supermassive black hole (SMBH) growth in galaxies? What is the role of orientation

and obscuration in the observed differences among certain AGN sub-classes? How is radio activity triggered? What is the origin of the tight scaling relations between the SMBH masses and various properties of their host spheroids? Ultimately, what is the link between galaxy and SMBH formation and evolution?

Quasars are the most powerful active galaxies. By studying their host galaxies at different redshift (z) we can investigate how the most massive black holes form and

* E-mail:jurbano@cab.inta-csic.es

evolve, what mechanisms trigger the most extreme form of nuclear activity and how this can affect the evolution of massive galaxies (Kormendi & Richstone 1995; Magorrian et al. 1998; Ferrarese et al. 2000; Gebhardt et al. 2000; Tremaine et al. 2002). Such studies have been focussed traditionally on type 1 (unobscured) quasars (QSO1). While some works proposed that QSO1 at low redshift ($z < 0.5$) are almost invariably hosted by massive, bulge-dominated galaxies (McLeod & Rieke 1994, 1995b; Dunlop et al. 2003; Lacy 2006; Hyvönen et al. 2007), other studies have shown a large diversity of hosts. A substantial disk component has been found in many galaxies hosting low- z quasars, with relative contribution to the total galaxy light possibly dependent on quasar luminosity and radio-loudness (Bahcall et al. 1997; Jahnke et al. 2004; Floyd et al. 2004; Bettoni et al. 2015).

In regard to the physical mechanisms that trigger AGN activity and SMBH growth, there is evidence supporting that a variety of processes can be involved, with the dominant one depending on AGN luminosity. While mergers of gas-rich galaxies are frequently suggested as the trigger for quasars, secular processes appear to be more relevant at lower AGN power (Toomre & Toomre 1972; Heckman et al. 1986; Combes 2001; Hopkins et al. 2006; Cisternas et al. 2011; Ramos-Almeida et al. 2011; Bessiere et al. 2012).

Host galaxy studies of type 2 (obscured) QSO (QSO2) at different z are currently of special relevance. This population is at least comparable in number density to the QSO1 population and perhaps 2-3 times larger (Tajer 2007; Gilli et al. 2011; Mateos et al. 2017). They are of great interest since they are signposts of vigorous obscured SMBH growth.

In comparison with QSO1 studies they can provide useful information regarding the QSO1 versus QSO2 unification scenario based on orientation (Antonucci 1993).

Only ~ 10 -15% of quasars are radio-loud. This applies to both QSO1 (Katgert et al. 1973; Fanti et al. 1977; Smith & Wright 1980) and QSO2 (Lal & Ho 2010). QSO2 studies offer the opportunity to characterize the host galaxies of the most luminous obscured radio-quiet AGN versus their radio-loud analogues, narrow line radio galaxies (NLRG, e.g. Dunlop et al. 2003; Best et al. 2005; Inskip et al. 2010).

QSO2 have been discovered in large numbers only recently (Zakamska et al. 2003). For this reason, studies of their hosts are scarce and have been focussed on small samples. Such studies have a clear advantage with respect to QSO1: the obscuration of the central engine renders a detailed view of the galaxies, allowing a more accurate morphological and structural characterization. These works suggest a diversity of galaxy host types, with a clear preference for ellipticals and bulge-dominated systems (Greene et al. 2009, Bessiere et al. 2012, Villar Martín et al. 2012, Kocevski et al. 2012, Wylezalek et al. 2016).

With the goal of shedding more light on this topic, we present here the results of the morphological and parametric characterization and subsequent classification of the host galaxies associated with 57 luminous obscured AGN at $z \sim 0.3$ -0.4. 41 are QSO2. In order to investigate the potential dependence of galaxy host properties with AGN power, 16 high-luminosity Seyfert 2 galaxies (HLSy2) are also part of this study (McLeod & Rieke 1995a, Kauffmann et al. 2003).

We also identify and classify merger/interaction features. Our study is based on Hubble Space Telescope (HST) optical images obtained with the Advanced Camera for Sur-

veys/Wide Field Channel (ACS/WFC) and the Wide Field Planetary Camera 2 (WFPC2). We have applied two different techniques: a visual classification and multi-parametric modelling, using GALFIT (Peng et al. 2010), which allows to isolate and parametrize the galaxy structural components.

The paper is organised as follows. The AGN sample and data are described in Section 2. The classification methods and the modelling procedure are explained in Section 3. The results of the visual and parametric classifications are presented in Section 4 and discussed in the context of related works in Section 5. Summary and conclusions are in Section 6.

We assume $\Omega_\Lambda = 0.73$, $\Omega_M = 0.27$ and $H_0 = 71 \text{ km s}^{-1} \text{ Mpc}^{-1}$.

2 SAMPLE AND DATA

The sample studied here consists of 57 luminous ($IO3 = \log(L_{[\text{OIII}]}/L_\odot) \geq 8.0$) type 2 AGN at $0.3 < z < 0.4$ from Zakamska et al. (2003) & Reyes et al. (2008) catalogues of Sloan Digital Sky Survey (SDSS) luminous type 2 AGN (Table 1).

Zakamska et al. (2003) selected 291 luminous type 2 AGN ($IO3 > 7.3$), at $z < 0.83$ from SDSS on the basis of their optical emission line properties: narrow emission lines ($\text{FWHM} < 2000 \text{ km s}^{-1}$) without underlying broad components, and optical line ratios typical of active galaxies, consistent with non-stellar ionizing radiation. Reyes et al. (2008) updated this catalogue based on ~ 3 times as much SDSS data. Their catalogue contains 887 luminous type 2 AGN ($IO3 > 7.9$), recovering $> 90\%$ of objects in Zakamska et al. (2003) in the same luminosity range. The spectra of the objects they missed tend to have low S/N or ambiguous classification.

About 744 (84%) objects in Reyes et al. (2008) have $IO3 \geq 8.3$ and are, therefore, QSO2. This threshold ensures the selection of objects with AGN luminosities in the quasar regime. Using $L_{[\text{OIII}]}$ as a proxy for AGN power (Heckman et al. 2004), the implied bolometric luminosities are above the classical Seyfert/quasar separation of $L_{\text{bol}} \sim 10^{45} \text{ erg s}^{-1}$. Only $\sim 15\% \pm 5\%$ QSO2 are expected to be radio-loud (Lal & Ho 2010).

The 57 AGN studied here are the sample of objects observed for the Hubble Space Telescope (HST) program 10880, with principal investigator Henrique Schmitt (Tables 1 and 2). HST imaging observations for other programmes exist for several more QSO2, but in general they have been done with different filters and/or the targets are at different z than our sample. Since the statistics will not improve significantly, these are not considered in our study.

There are 97 SDSS QSO2 and 36 HLSy2 in the $0.3 < z < 0.4$ range. Of these, our subsample contains 41 ($\sim 42\%$) QSO2 and 16 HLSy2 ($\sim 44\%$). Although uncertainties remain regarding the exact selection criteria applied by the team responsible for the 10880 HST program, based on the high fractions quoted above we consider they are an adequate representation of the total sample of SDSS QSO2 and HLSy2 in these z and $L_{[\text{OIII}]}$ ranges.

The ACS/WFC and WFPC2 images used in this work are from the Hubble Legacy Archive (HLA)¹.

3 CLASSIFICATION METHODS

We have classified the host galaxies based on two main methods: visual and parametric.

The visual inspection of host galaxy images provides a classification based on their apparent morphology. It has been a standard practice for more than 80 years (Hubble 1936) and is contributing still today to achieve a deeper understanding of galaxy evolution (Lintott 2008, Nair & Abraham 2010, Willett et al. 2013). A limitation of this method is that it can be subjective, so that the same object can be classified differently by different observers. Frequently, it does not allow to determine which structural component (disk or bulge) dominates the total galaxy light, thus preventing an accurate classification. A more robust classification needs to be based on a multi-parametric modelling approach. This allows to extract structural components from galaxy images, by modeling their light profiles (Peng et al. 2010). This method has also limitations. As an example, complex mergers can be missclassified by applying a too simplistic approach of assuming that all galaxies consist of a disk and/or a spheroidal component. Visual inspection is particularly useful in these cases.

Both methods have been essential in our work: the visual classification has allowed to identify complex mergers that cannot be classified neither as bulge or disk dominated systems. It has also been useful to disentangle the parametric classification in a minority of bulge or disk dominated cases where the parametric method resulted on degenerate fits.

More details on the classification methods are provided next.

3.1 Visual classification

We have applied three different methods of visual classification:

- Method Vis-I. Three groups have been considered: spiral and disks with not obvious spiral arms, ellipticals and highly-disturbed systems. These are systems of very complex morphologies due to merger/interaction processes which cannot be classified in the previous two groups.

- Method Vis-II focuses on the identification of features indicative of galaxy interactions.

Given that QSO2 host galaxies are often associated with morphological features indicative of past or ongoing merger/interaction events (Villar Martín et al. 2012; Bessiere et al. 2012), we have classified our objects to highlight the presence of such features, adopting the following schemes of Rodríguez Zaurín et al. (2011) and Veilleux et al. (2002):

- Class 0: Objects that appear to be single isolated galaxies, dominated by a relatively symmetric morphology with no peculiar features.

- Class 0*: Objects that appear to be single isolated galaxies, dominated by a symmetric morphology with some faint irregular morphological features such as tails, shells, etc (see Method Vis-III below).

- Class 1: objects in a pre-coalescence phase with two well differentiated nuclei separated a projected distance >1.5 kpc. For these objects, it is still possible to identify the individual merging galaxies and their corresponding tidal structures due to the interaction.

- Class 2: objects with two nuclei separated a projected distance ≤ 1.5 kpc or a single nucleus with an asymmetric morphology and prominent irregular features suggesting a post-coalescence merging phase.

- Method Vis-III. Morphological appearance of peculiar features. To further refine this classification, we have also characterized the morphological appearance of the merger/interaction features following Ramos-Almeida et al. (2011): T: tidal tail; F: Fan; B: Bridge; S: Shell; D: dust feature; 2N: Dual-Core/Double Nucleus; A: amorphous halo; I: irregular feature; IC: interacting companion. We have added: K: Knot, as an extra feature for the characterization.

In this paper we present the results of all three visual methods, although we will focus the scientific discussion on Method Vis-I.

3.2 Parametric classification

The two dimensional (2D) fitting algorithm GALFIT (version 3.0) has been used to model the galaxies. This algorithm allows to extract structural components of galaxies by modelling their light profiles with parametric functions (Peng et al. 2002, 2010). The final fit for each galaxy consists of one or more components. One may be a point source (a point spread function, PSF) and the rest are described by a Sérsic (1963) function:

$$\Sigma(r) = \Sigma_e e^{-\kappa[(r/r_e)^{1/n}-1]} \quad (1)$$

where r_e is the effective radius of the galaxy, Σ_e is the surface brightness at radius $r = r_e$, n is the Sérsic index and κ is a parameter coupled to n so that half of the total flux is within r_e . The particular cases of $n = 4$ (Vaucouleurs' law) and $n = 1$ are often assumed to fit bulge and exponential disk components respectively.

GALFIT fits the following parameters for each Sérsic component: central position (x, y) , integrated magnitude $(MAG)^2$, r_e , n , axis ratio (b/a) and position angle of the major axis (PA) . The users need to start the algorithm with initial guesses for these parameters, that have to be as accurate as possible, and a value for the sky background. Following different works (Häußler et al. 2007, Buitrago et al. 2008, 2017), we obtain the input parameters with SEXTRACTOR (Bertin & Arnouts 1996) except the sky background (see Sect. 3.2.2). Zero points are fixed in each object and they are provided in Table 2. Close neighbours were fitted using Single Sérsic profiles simultaneously with the target

¹ <https://hla.stsci.edu/>

² Correction for Galactic extinction has been taken into account

Object SDSS Name [1]	z [2]	Scale kpc/arcsec [3]	$lO3$ [4]	Instrument /filter [5]	Date dd/mm/yr [6]	AGN Classification [7]	Emission lines [8]
J002531.46-104022.2	0.303	4.45	8.73	ACS/F775W	11/09/06	QSO2	H α , [NII] doublet
J005515.82-004648.6	0.345	4.86	8.15	WFPC2/F814W	18/06/07	HLSy2	H α , [NII] doublet
J011429.61+000036.7	0.389	5.25	8.66	ACS/F775W	07/08/06	QSO2	[OIII] 4959,5007
J011522.19+001518.5	0.390	5.26	8.14	WFPC2/F814W	11/06/07	HLSy2	H α , [NII] doublet
J014237.49+144117.9	0.389	5.25	8.76	ACS/F775W	11/08/06	QSO2	[OIII] 4959,5007
J015911.66+143922.5	0.319	4.61	8.56	ACS/F775W	12/08/06	QSO2	No
J020234.56-093921.9	0.302	4.44	8.39	WFPC2/F814W	18/06/07	QSO2	H α , [NII] doublet
J021059.66-011145.5	0.384	5.21	8.10	WFPC2/F814W	25/06/07	HLSy2	H α , [NII] doublet
J021758.18-001302.7	0.344	4.85	8.55	ACS/F775W	19/10/06	QSO2	No
J021834.42-004610.3	0.372	5.10	8.85	ACS/F775W	15/09/06	QSO2	[OIII] 5007
J022701.23+010712.3	0.363	5.02	8.90	ACS/F775W	06/11/06	QSO2	[OIII] 5007
J023411.77-074538.4	0.310	4.52	8.77	ACS/F775W	30/10/06	QSO2	H α , [NII] doublet
J031946.03-001629.1	0.393	5.22	8.24	WFPC2/F814W	25/11/08	HLSy2	H α , [NII] doublet
J031927.22+000014.5	0.385	5.28	8.06	WFPC2/F814W	25/11/08	HLSy2	H α , [NII] doublet
J032029.78+003153.5	0.384	5.21	8.52	ACS/F775W	11/11/06	QSO2	[OIII] 4959, 5007
J032533.33-003216.5	0.352	4.93	9.06	WFPC2/F814W	26/11/08	QSO2	H α , [NII] doublet
J033310.10+000849.1	0.327	4.69	8.13	WFPC2/F814W	25/11/08	HLSy2	H α , [NII] doublet
J034215.08+001010.6	0.348	4.89	9.08	WFPC2/F814W	22/11/08	QSO2	H α , [NII] doublet
J040152.38-053228.7	0.320	4.62	8.96	WFPC2/F814W	28/11/08	QSO2	H α , [NII] doublet
J074811.44+395238.0	0.372	5.10	8.19	WFPC2/F814W	20/11/08	HLSy2	H α , [NII] doublet
J081125.81+073235.3	0.350	4.91	8.88	WFPC2/F814W	22/11/08	QSO2	H α , [NII] doublet
J081330.42+320506.0	0.398	5.33	8.83	ACS/F775W	16/12/06	QSO2	[OIII] 4959, 5007
J082449.27+370355.7	0.305	4.47	8.28	WFPC2/F814W	23/11/08	QSO2	H α , [NII] doublet
J082527.50+202543.4	0.336	4.78	8.88	WFPC2/F814W	20/11/08	QSO2	H α , [NII] doublet
J083028.14+202015.7	0.344	4.85	8.91	WFPC2/F814W	20/11/08	QSO2	H α , [NII] doublet
J084041.08+383819.8	0.313	4.55	8.47	WFPC2/F814W	21/11/08	QSO2	H α , [NII] doublet
J084309.86+294404.7	0.397	5.32	9.34	WFPC2/F814W	21/11/08	QSO2	[OIII] 5007, H α , [NII] doublet
J084856.58+013647.8	0.350	4.91	8.46	ACS/F775W	08/10/06	QSO2	No
J084943.82+015058.2	0.376	5.14	8.06	WFPC2/F814W	26/11/08	HLSy2	H α , [NII] doublet
J090307.84+021152.2	0.329	4.71	8.42	WFPC2/F814W	26/11/08	QSO2	H α , [NII] doublet
J090414.10-002144.9	0.353	4.94	8.93	ACS/F775W	11/12/06	QSO2	No
J090801.32+434722.6	0.363	5.02	8.31	WFPC2/F814W	21/11/08	QSO2	H α , [NII] doublet
J092318.06+010144.8	0.386	5.23	8.94	WFPC2/F814W	21/11/08	QSO2	H α , [NII] doublet
J092356.44+012002.1	0.380	5.17	8.59	WFPC2/F814W	17/11/08	QSO2	H α , [NII] doublet
J094209.00+570019.7	0.350	4.91	8.31	WFPC2/F814W	22/11/08	QSO2	H α , [NII] doublet
J094350.92+610255.9	0.341	4.82	8.46	WFPC2/F814W	15/04/07	QSO2	H α , [NII] doublet
J095629.06+573508.9	0.361	5.01	8.38	WFPC2/F814W	26/11/08	QSO2	H α , [NII] doublet
J100329.86+511630.7	0.324	4.66	8.11	WFPC2/F814W	26/11/08	HLSy2	H α , [NII] doublet
J103639.39+640924.7	0.398	5.33	8.42	WFPC2/F814W	14/04/07	QSO2	[OIII] 5007, H α , [NII] doublet
J112907.09+575605.4	0.313	4.55	9.38	WFPC2/F814W	26/11/08	QSO2	H α , [NII] doublet
J113710.78+573158.7	0.395	5.30	9.61	WFPC2/F814W	26/11/08	QSO2	[OIII] 5007, H α , [NII] doublet
J133735.01-012815.7	0.329	4.71	8.72	WFPC2/F814W	04/04/07	QSO2	H α , [NII] doublet
J140740.06+021748.3	0.309	4.51	8.90	WFPC2/F814W	05/04/07	QSO2	H α , [NII] doublet
J143027.66-005614.9	0.318	4.60	8.44	WFPC2/F814W	05/04/07	QSO2	H α , [NII] doublet
J144711.29+021136.2	0.386	5.23	8.45	WFPC2/F814W	02/05/07	QSO2	H α , [NII] doublet
J150117.96+545518.3	0.338	4.79	9.06	WFPC2/F814W	08/04/07	QSO2	H α , [NII] doublet
J154133.19+521200.1	0.311	4.53	8.25	WFPC2/F814W	02/04/07	HLSy2	H α , [NII] doublet
J154337.81-004420.0	0.311	4.53	8.40	WFPC2/F814W	05/05/07	QSO2	H α , [NII] doublet
J154613.27-000513.5	0.383	5.20	8.18	WFPC2/F814W	03/05/07	HLSy2	H α , [NII] doublet
J172419.89+551058.8	0.365	5.04	8.00	WFPC2/F814W	17/05/07	HLSy2	H α , [NII] doublet
J172603.09+602115.7	0.333	4.75	8.57	WFPC2/F814W	08/04/07	QSO2	H α , [NII] doublet
J173938.64+544208.6	0.384	5.21	8.42	WFPC2/F814W	10/04/07	QSO2	H α , [NII] doublet
J214415.61+125503.0	0.390	5.26	8.14	WFPC2/F814W	14/05/07	HLSy2	H α , [NII] doublet
J215731.40+003757.1	0.390	5.26	8.39	WFPC2/F814W	12/05/07	QSO2	H α , [NII] doublet
J223959.04+005138.3	0.384	5.21	8.15	WFPC2/F814W	17/05/07	HLSy2	H α , [NII] doublet
J231755.35+145349.4	0.311	4.53	8.10	WFPC2/F814W	21/05/07	HLSy2	H α , [NII] doublet
J231845.12-002951.4	0.397	5.32	8.00	WFPC2/F814W	12/06/07	HLSy2	[OIII] 5007, H α , [NII] doublet

Table 1. List of objects observed for the HST program 10880. Col(3) quotes the kpc/arcsec conversion. The [OIII] luminosity in Col(4), $lO3$, is given in log and relative to the solar luminosity (Reyes et al. 2008). Objects with $lO3 \gtrsim 8.3$ are type 2 quasars (QSO2) in Col(7). Objects with lower values are classified as high-luminosity Seyfert 2s (HLSy2). Col(5): HST instrument and filter. Col(6): Date of observation. Col(8): Emission lines contaminating the filter.

galaxies to avoid contamination of the AGN host light profiles.

GALFIT provides r_e and MAG of the individual components, but not the global values for the galaxy. To obtain these, elliptical isophotes were fitted to the galaxy's 2D model using the ELLIPSE task in IRAF. To avoid overestimations of the total galaxy flux F_T and of r_e , the outer model isophote was carefully fixed to coincide with the HST image isophote for which the flux per pixel is $>3\sigma$ (Section 3.2.2). The relative contribution of each structural component is measured as the flux within this isophote relative to F_T , $\frac{F_i}{F_T}$. The galaxy r_e is taken as the major axis of the model isophote that contains $\frac{F_T}{2}$ (Table 3).

3.2.1 PSF

We refer the reader to the Appendix A for a detailed description and discussion on the PSF construction method.

3.2.2 Determination of the sky background

An accurate determination of the sky background is essential, especially for faint objects and galaxies with extended low surface brightness structures.

Following Häußler et al. (2007) we introduced the background level as a fixed parameter of GALFIT. To calculate it for each AGN image, we selected emission free areas (i.e. masking sources) around the object to avoid contamination. The sky background was then estimated as the average value of all pixels with values $< 3\sigma$, after applying a 3σ clipping method.

3.2.3 Methodology

We have followed two steps to obtain the parametric fits:

- Method Par-I. The light profile and global morphology are parametrized using a single Sérsic component. This method has been used in numerous works (Weinzirl et al. 2009, Buitrago et al. 2013, Davari et al. 2016) to classify galaxies depending on n into spheroidal or disk galaxies.

As we will see (Sect. 4.2), single Sérsic profiles do not provide acceptable fits in the majority of our objects. This method has been useful, on the other hand, to obtain a preliminary guess of the galaxy types and to constrain the input parameters of GALFIT when applying more complex fits (Method Par-II). It has also proved useful to identify objects where the contribution of a point source is necessary. It is found that whenever a single Sérsic component fit resulted on a $n \geq 8$, the contribution of a point source is confirmed by the more sophisticated Method Par-II. The point source contribution may be relatively low in flux, but it can modify the shape of the inner light profile significantly.

- Method Par-II. Two or more components are considered in the fit with the goal of isolating and parametrizing different constituents and, when necessary, to separate overlapping galaxies. The combination can include two or more Sérsic components and, if necessary, a point source. All are

combined to reproduce the global light profile of a given galaxy.

For a given object, we select the fit with the minimum number of components that best reproduces the surface brightness profile and leaves minimum residuals in the 2D residual image, excluding asymmetric peculiar features. We find that all galaxies can be successfully fitted with a maximum of three components: a point source and two Sérsic profiles.

3.2.4 Physical nature of the structural components

One of our main aims is to classify the galaxies according to the structural component that dominates the galaxy luminosity (i.e. bulge-dominated, disk-dominated, other). It is necessary to define some criteria to associate each component with a physical counterpart.

We assume $n = 1$ for disks. This is a common practice which is justified by the fact that the light profile of disks is indeed exponential (Freeman 1970). The situation is less simple for bulges and elliptical galaxies. Although the $r^{1/4}$ de Vaucouleurs profile is often assumed, numerous works have shown that this must be generalized to $r^{1/n}$ to account for the range of values of n spanned by different galaxies (Trujillo et al. 2001; Häußler et al. 2007; Allen et al. 2006; Ribeiro et al. 2016). Following Gadotti (2009) (see also Barentine & Kormendy 2012) we will consider that a $n \geq 2$ Sérsic is a bulge.

Peculiar features are frequent around high-luminosity AGN (e.g. tidal tails, fans, etc). This is also the case for our sample (Villar Martín et al. 2012; see also 4.1.2). When such features are irregular and asymmetric, they are easily recognized in the residual images. However, when they are diffuse and symmetric, GALFIT may reproduce them successfully with low $n \leq 1$ Sérsic components, which may be erroneously interpreted as disks or bars ($n \sim 0.5$, Peng et al. 2002). To avoid such degeneracy (which we find to affect a minority of objects anyway), we have carefully checked for every target whether the interpretation of the nature of the different structural components revealed by the fit is coherent with the visual inspection.

Taking into account all these considerations, the galaxies will be classified as follows:

- Highly-disturbed systems. This group contains objects with strongly distorted morphologies with clear signs of galactic interactions, according to the classification described in Sect. 3.1. These objects cannot be fitted with GALFIT accurately.

- Point-source-dominated objects. A point source contributes $>50\%$ to the total galaxy flux.

- Objects with a single Sérsic component (with or without point source). The objects will be classified in terms of n following Graham et al. (2005) (see also Häußler et al. 2007).

- $n < 2$. Disk-like. These will be considered *disk-dominated* systems.

- $n \geq 2$. Spheroidal. These will be considered *bulge-dominated* systems.

- Objects with two Sérsic components (with or without point source).

Instrument	Pixel scale arcsec pix ⁻¹	FWHM(PSF) arcsec	FWHM(PSF) kpc	Filter	$\Delta\lambda$ Å	Z_p	Nr. of objects
[1]	[2]	[3]	[4]	[5]	[6]	[7]	[8]
ACS/WFC	0.05	0.12	0.54-0.65	F775W	6804-8632	25.65	12
WFCP2	0.1	0.25	1.1-1.4	F814W	6984-10043	24.21	45

Table 2. Instrument specifications. [4]: range of PSF physical sizes spanned by the z of the sample. [6]: spectral range covered by the filter. [7]: Zero point values for flux calibration (Lucas et al. 2016). [8]: Number of objects observed with each instrument.

Object SDSS Name [1]	$IO3$ [2]	Magnitude (mag)		Hr SETRACTOR (kpc) [5]	R_{eff} GALFIT (kpc) [6]
		SETRACTOR [3]	GALFIT [4]		
J005515.82-004648.6	8.15	19.3	19.3	1.5	1.5
J011429.61+000036.7	8.66	17.7	17.5	5.5	5.9
J011522.19+001518.5	8.14	18.1	18.1	7.8	4.5
J014237.49+144117.9	8.76	17.8	17.8	1.1	1.1
J015911.66+143922.5	8.56	19.7	19.5	1.4	1.2
J020234.56-093921.9	8.39	17.4	17.6	7.1	6.3
J021059.66-011145.5	8.10	19.0	19.0	3.8	3.0
J023411.77-074538.4	8.77	18.7	18.7	2.2	2.3
J031946.03-001629.1	8.06	18.9	18.8	6.3	7.5
J031927.22+000014.5	8.24	19.1	18.8	4.2	4.5
J032029.78+003153.5	8.52	17.3	17.0	10.0	12.8
J034215.08+001010.6	9.08	19.3	19.2	1.2	1.1
J040152.38-053228.7	8.96	18.9	19.0	2.8	2.7
J074811.44+395238.0	8.19	18.9	18.7	4.5	4.6
J081125.81+073235.3	8.88	19.1	19.2	5.5	4.0
J082449.27+370355.7	8.28	19.2	19.0	1.2	1.3
J082527.50+202543.4	8.88	19.7	19.7	0.9	1.1
J083028.14+202015.7	8.91	18.6	18.5	2.2	2.5
J084041.08+383819.8	8.47	17.9	17.8	6.3	7.1
J084309.86+294404.7	9.34	18.8	18.7	3.9	3.1
J084856.58+013647.8	8.46	17.8	17.1	6.1	4.9
J084943.82+015058.2	8.06	19.5	19.5	1.9	2.2
J090414.10-002144.9	8.93	17.9	17.8	2.8	2.9
J092318.06+010144.8	8.94	18.9	18.8	3.6	3.1
J094209.00+570019.7	8.31	18.9	18.7	1.8	1.6
J094350.92+610255.9	8.46	19.5	19.6	1.0	1.0
J095629.06+573508.9	8.38	19.1	19.0	2.8	3.2
J100329.86+511630.7	8.11	18.4	18.4	5.2	4.8
J103639.39+640924.7	8.42	18.1	17.8	7.5	7.3
J112907.09+575605.4	9.38	19.3	19.1	2.0	2.4
J113710.78+573158.7	9.61	19.1	18.6	3.0	3.3
J140740.06+021748.3	8.90	19.3	19.2	1.4	1.5
J150117.96+545518.3	9.06	17.2	17.2	6.2	6.1
J154133.19+521200.1	8.25	17.8	18.0	7.9	6.7
J154613.27-000513.5	8.18	19.3	19.0	3.8	3.8
J172419.89+551058.8	8.00	19.5	19.3	1.5	1.4
J172603.09+602115.7	8.57	19.8	19.8	1.2	1.2
J173938.64+544208.6	8.42	19.3	19.2	2.1	2.6
J214415.61+125503.0	8.14	18.4	18.5	1.9	1.2
J223959.04+005138.3	8.15	18.9	18.9	3.7	3.6
J231755.35+145349.4	8.10	18.4	18.3	6.7	6.2
J231845.12D-002951.4	8.00	18.6	18.4	5.6	4.3

Table 3. Comparison between the total magnitude and the half-radius calculated with SETRACTOR and the effective radius inferred with the task ELLIPSE applied to the GALFIT 2D model image. Only objects that could be fitted with GALFIT are shown. The SETRACTOR values were obtained by applying the code to the HST data. The GALFIT mag and R_{eff} values were measured in the best fit model image.

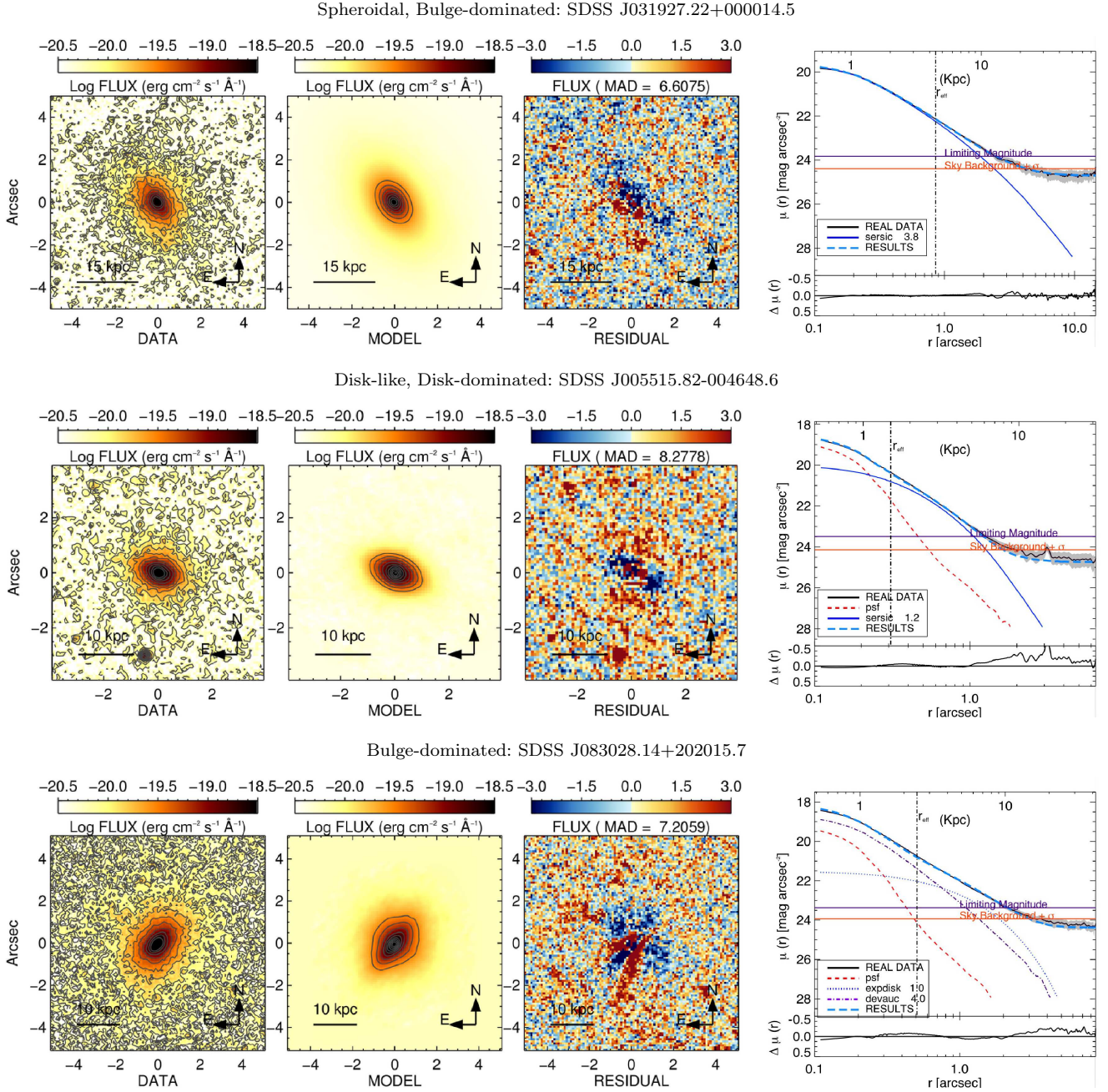


Figure 1. Examples of GALFIT decomposition method. The 2D images are, from left to right: the HST data, the model and the residual image. Ten contours are plotted in the two first images, with values evenly distributed in the range 3σ to the maximum flux of the object of interest. The colour scale of the residual images varies within the range $-3MAD$ and $+3MAD$ (see Sect. 3.2.5). The plots on the right panel show the 1D light profile of both data and model, and the individual structural components. The following convention has been adopted: data (black solid line), best fit (light blue long-dashed line, labelled “RESULTS” in the plots). In addition, a red dashed line will be always used for point sources; a blue dotted line for disks ($n=1.0$); a purple dash-dotted line for De Vaucouleur profiles (i.e. fixed $n=4.0$); blue solid lines are used for Sérsic components of free n , independently of this index value. The vertical lines mark the effective radius of the model image. The orange and purple horizontal lines indicate the background level plus σ (the standard deviation of the sky background, both calculated in section 3.2.2) and the limiting magnitude, respectively, calculated as $-2.5 \times \log(\text{sky background} + \sigma) + Zp + 5 \times \log(\text{pix scale})$ and $-2.5 \times \log(\text{sky background} + 3 \times \sigma) + Zp + 5 \times \log(\text{pix scale})$. The grey shadowed area represents the data Poisson errors. Bottom panel, inset: the residuals of the fit $\Delta \text{MAG} = \text{MAG}(\text{DATA}) - \text{MAG}(\text{FIT})$ at each radial distance are shown.

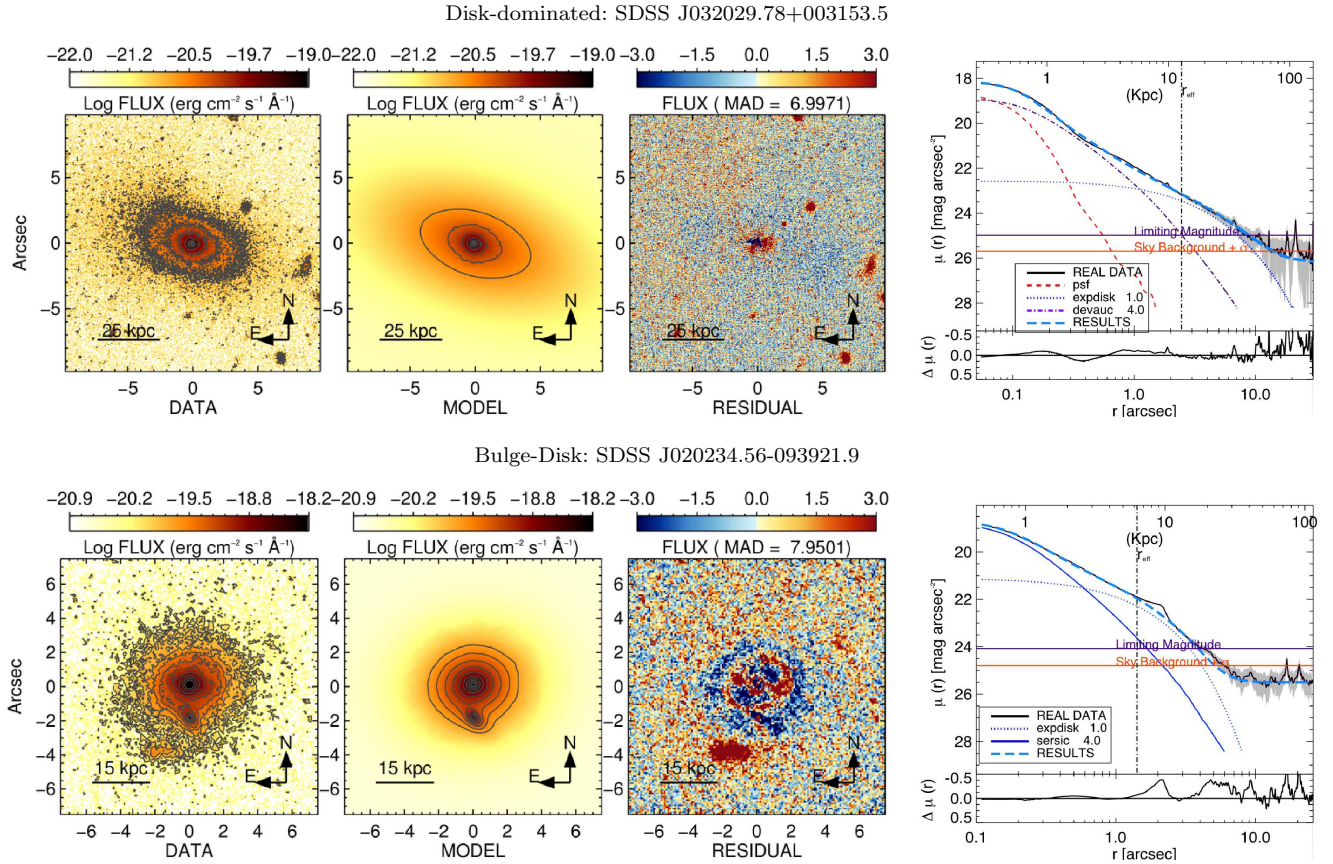


Figure 1 (Cont.).

– Systems with $B/D < 0.8$ will be classified as *disk-dominated*. The disk-component ($n = 1$) contributes more than the bulge ($n \geq 2$).

– Systems with $B/D > 1.2$ will be classified as *bulge-dominated*. The bulge-component contributes more than the disk.

– Systems with $B/D = 1.0 \pm 0.2$, will be classified as *bulge+disk* systems. The disk and the bulge have similar contribution.

3.2.5 Selection of the best fit

Our final parametric galaxy classification is based on Method Par-II (see Section 3.2.3 and Tables 5 and 6). We explain next the criteria adopted to select the best fit for each object.

Five examples are shown in Fig. 1. For each object the HST HLA image, the 2D GALFIT model and the residual image are shown on the left panels. The surface brightness profile, the best fit, the profiles of the individual structural components and the residuals (data - model) are plotted in the right panel.

The residual 2D image has been created as follows. The best fit model was subtracted from the original image producing a residual image *res*. This was then divided by MAD (the median absolute deviation) calculated using regions with no bright objects or features. Pixels with absolute values $|F| = \left| \frac{res}{MAD} \right| < 3$ keep their values and they

will be considered to be within the noise level. Pixels with $|F| \geq 3$ are replaced by +3 or -3 depending on the F sign. These residuals are potentially real (at or above the detection limit), except possibly in the central region of galaxies, since a small spatial shift of a fraction of a pixel of the PSF relative to the galaxy centre can produce strong artificial residuals. The colour scale in the final residual image presented in the figures is in the range $-3 \times MAD$ to $+3 \times MAD$.

Multiple combinations of structural components were attempted based on different assumptions: from the standard $n = 1$ (disks) and $n = 4$ (bulges), to combinations of free n components, including or not a point source.

The selection of the best fit for each object is based on the following criteria/checks:

- The fit consists of the minimum number of components that best reproduces the surface brightness profile and leaves minimum residuals in the 2D residual image, excluding peculiar features that are confirmed to be real.
- Fits requiring Sérsic components whose contribution to the total flux is $< 10\%$ (> 2.5 magnitudes difference relative to the total magnitude) are rejected. It is found that these components have always low n and do not result in significant changes in the fit. This does not apply to the point source: since its profile is very steep (high n), even a small contribution of \sim a few % can change significantly the shape of the central regions of the galaxies.
- All fits were visually inspected and compared with the original image. This was sometimes very useful, for instance,

to confirm the presence of disks; also to check whether low n components are bars/disks or, alternatively, peculiar diffuse features (Sect. 3.2.4).

- An additional test that helped to refine (even discard) some fits was applied as follows. A region centred on the galaxy centroid and of typical size ~ 25 pixels \times 25 pixels (2.5×2.5 arcsec² for the WFPC2 and 1.25×1.25 arcsec² for the ACS) is selected both in the original and the residual images. The pixel with maximum value, F_{\max} is identified in the HST image. We then calculate $\Delta_{\max} = \frac{F_{\max} - F'_{\max}}{F_{\max}}$, where F'_{\max} is the flux value of that same pixel in the residual image and $\Delta_{\min} = \frac{F_{\max} + F'_{\min}}{F_{\max}}$, where F'_{\min} is the minimum value measured in the same area in the residual image. When Δ_{\max} or Δ_{\min} are larger than 0.5, the fits are further inspected. Such large deviations, warn about possible problems with the centring, the possible need for a point source or the presence of peculiar features such as prominent dust lanes. These objects were analyzed with special care to identify whether the strong residuals are real or artefacts.

4 RESULTS

4.1 Morphological Visual classification

4.1.1 Method Vis-I

We show in Table 6 (column [3]) and Fig. 2 the results of the visual classification based on Method Vis-I described in Sect. 3.1. Owing to the small sample size, we estimate the 1σ confidence intervals of the different galaxy populations studied here following a similar method as in Cameron (2011). In our case we use a Dirichlet distribution, a multivariate generalization the Beta binomial distribution, which provides a better performance at low sampling conditions compared to other methods such as the ‘normal approximation’ and the Clopper & Pearson (1934) approach (see Cameron 2011 for more details).

The main results are:

- Among QSO2, 27/41 or $66\%_{-10}^{+5}$ are visually classified as ellipticals, 5/41 or $12\%_{-4}^{+7}$ are spirals or disks and 9/41 or $22\%_{-6}^{+7}$ are highly-disturbed systems (HD). Among HLSy2, 9/16 or $56\%_{-15}^{+9}$ are ellipticals, 6/16 or $38\%_{-12}^{+10}$ are spirals or disks and 1/16 or $6\%_{-3}^{+11}$ is a HD.
- Thus, a minority of QSO2 are hosted by disk/spirals. This fraction is significantly higher in the HLSy2 subsample.
- There is tentative evidence for the fraction of HD to be higher in QSO2 than in HLSy2, although taking uncertainties into account the difference is not significant.

4.1.2 Methods Vis-II and Vis-III

The previous visual method does not allow the identification of all objects with signs of mergers/interactions, but only the most morphologically disturbed systems. However, their identification can be done with the classification method Vis-II (see Sect. 3.1). The results are shown in Fig. 3 (see also Table 6, column [4]).

The first result is that QSO2 and HLSy2 are distributed quite evenly among the 4 classes, from isolated objects, without (Class 0) or with (Class 0*) peculiar features, to objects with signatures of galaxy interactions at different stages

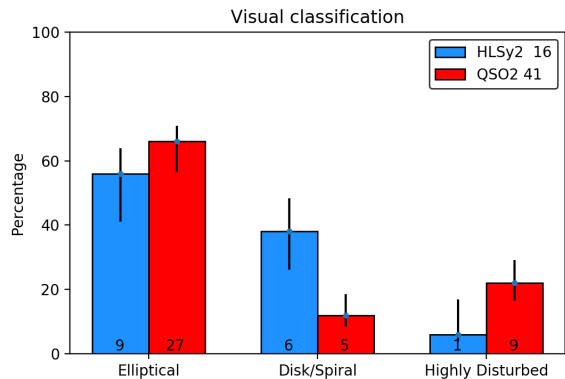


Figure 2. Results of the visual classification Method Vis-I (Sect. 3.1). The numbers within the bins in this and other histograms are the actual number of objects classified within each specific bin. The error bars in this and all histograms are 1σ Dirichlet multinomial distribution confidence intervals.

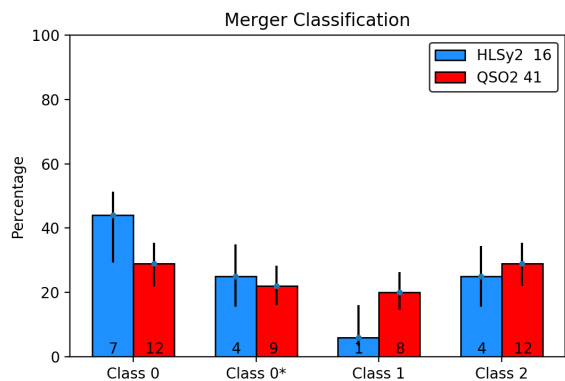


Figure 3. Results of the visual classification Method Vis-II (Sect. 3.1), which is focused on the evidence of merger/interactions. Numbers within the bins and error bars as in Fig. 2.

(Classes 1 and 2). This means that powerful nuclear activity occurs both in isolated objects and at different phases of galactic interactions, as already found in different studies such as Ramos-Almeida et al. (2011) and Bessiere et al. (2012).

The additional classification of the peculiar features based on Ramos-Almeida et al. (2011) (Method Vis-III) provides complementary information: $71\%_{-8}^{+6}$ of QSO2 show peculiar features that have been classified according to their aspect in column [5] of Table 6. For the HLSy2 sub-sample the percentage is $56\%_{-13}^{+12}$. These values may be lower limits, given the higher difficulty to identify peculiar features in galaxies with spiral/disk structures.

Bessiere et al. (2012) studied and classified the peculiar features in a complete sample of 20 SDSS QSO2 at $0.30 < z < 0.41$ and with $lO3 \geq 8.5$. 13 of these are also in our sample. They used deep Gemini Multi-Object Spectrograph-South optical broad-band images obtained with the r' -band filter (r_{G0326} , $\lambda_{\text{eff}} = 6300\text{\AA}$, $\Delta\lambda = 1360\text{\AA}$). They found that $\sim 75\%$ of their QSO2 show evidence for peculiar features. If

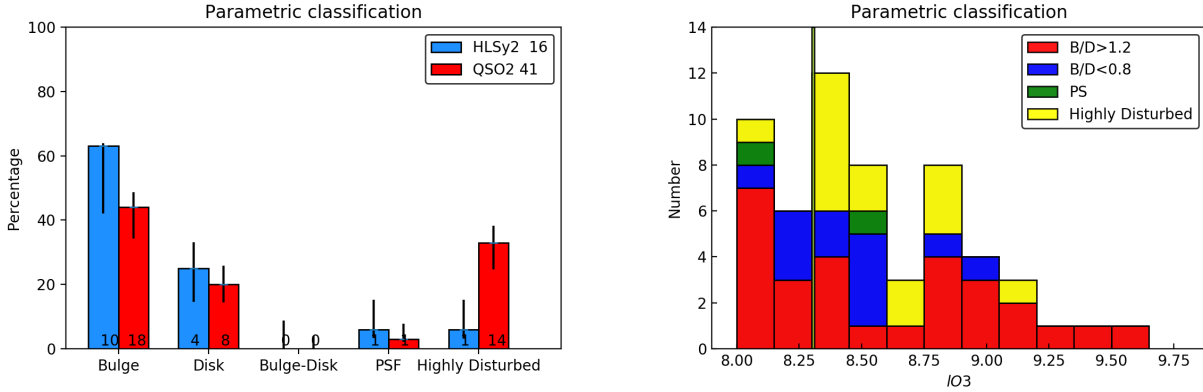


Figure 4. *Left:* Results of the parametric classification for QSO2 and HLSy2. “Bulge” are bulge-dominated systems, which include galaxies with $B/D > 1.2$ and spheroidal systems (single Sérsic with $n \geq 2$). “Disk” are disk-dominated systems, which include galaxies with $B/D < 0.8$ and disk like systems (single Sérsic with $n < 2$). “Bulge-Disk” are systems for which $0.8 \leq B/D \leq 1.2$ (zero found in the sample) and “PSF” are systems where a point source contributes $\geq 50\%$ of the total light. The numbers within the bins and the error bars are explained in Fig. 2 *Right:* Dependence of the galaxy classification with $L_{[\text{OIII}]}$ (proxy of AGN power). For each luminosity bin, the number of galaxies classified within a certain class is indicated by the height of the corresponding coloured rectangle. For instance, in the the $IO3 \sim 8.25$ bin there are 3 bulge-dominated and 3 disk-dominated galaxies. The vertical line corresponds to $IO3 = 8.3$, assumed as the dividing value between HLSy2 and QSO2.

we focus on those objects in the HST sample with $IO3 \geq 8.5$, we find the same rate as them: $75\%_{-11}^{+7}$ show peculiar features.

Considering the 13 QSO2 that overlap with our study, Bessiere et al. (2012) confirm peculiar features in 11 objects. We confirm them in 10. The discrepant object is SDSS J011429.61+000036.7. They identify a second nucleus (which, given the unknown z , we have classified as projected companion “PC”) and a shell which is not clearly detected in the HST image.

4.2 Parametric classification

Following Sect. 3.2, we classify the host galaxies of our sample based on the dominant structural component identified as a result of the parametric fits. This method could not be applied to 15/57 objects, of which 14 are QSO2 and 1 is HLSy2. In general, they present strongly distorted morphologies. These objects will be referred to as “highly-disturbed” (HD), in coherence with the visual classification. The results of the parametric method for individual objects are shown in Table 6. The distribution of the sample among the different classification groups is shown in Tables 7 and 8, and in Fig. 4 (left). The difference between these two tables is that Table 7 includes HD systems, while Table 8 does not.

The main results are:

- **Bulge-dominated systems:** This group includes spheroidal galaxies or galaxies with $B/D > 1.2$ (Sect. 3.2.4). It is the most numerous group both for QSO2 (18/41 or $44\%_{-10}^{+5}$) and for HLSy2 (10/16 or $63\%_{-21}^{+1}$). Taking uncertainties into account, no significant difference between QSO2 and HLSy2 is found.

If HD are excluded, no significant difference is found either (18/27 or $67\%_{-15}^{+4}$ for QSO2 and HLSy2 (10/15 or $67\%_{-21}^{+3}$).

- **Disk-dominated systems:** These are disk-like galaxies or galaxies with $B/D < 0.8$ (Sect. 3.2.4). Only $25\%_{-11}^{+8}$ (4/16)

of HLSy2 and $20\%_{-6}^{+6}$ (7/41) of QSO2 galaxies are disk-dominated. The difference between both groups is not significant.

If HD systems are excluded the fractions become 4/15 or $27\%_{-11}^{+10}$ for HLSy2 and 8/27 or $\sim 29\%_{-9}^{+8}$ for QSO2.

- **Bulge+disk systems ($B/D = 1.0 \pm 0.2$)** have not been found ($0\%_{-9}^{+9}$ of HLSy2 and $0\%_{-3}^{+3}$ of QSO2).

- **Disks (not necessarily dominating the total galaxy flux)** are identified in a significantly higher fraction of HLSy2 (7/16 or $44\%_{-11}^{+13}$) than QSO2 (10/41 or $24\%_{-6}^{+8}$).

If HD systems are excluded, the difference between both fractions disappears: HLSy2 ($47\%_{-12}^{+13}$) and QSO2 ($37\%_{-8}^{+10}$) have disks.

- **A point source component is isolated in a high fraction of objects:** 29 (10 HLSy2 and 19 QSO2) of the 42 ($69\%_{-8}^{+7}$) for which the parametric analysis could be applied, with no significant difference between both groups. The relative contribution to the total flux varies between 3% and 51%, with average value $20.7 \pm 2.9\%$ (median 14.2%). The PSF dominates ($\geq 50\%$ of the total flux) in just one HLSy2 and one QSO2.

4.3 Dependence of galaxy host with $IO3$

We have seen that, excluding highly-disturbed systems, the parametric classification of the HLSy2 and QSO2 hosts are consistent within the errors.

We perform next a more detailed analysis of the dependence of galaxy properties with $IO3$, proxy for AGN power. For this, we use a finer sampling of the line luminosity range, instead of the coarse and somewhat arbitrary division in HLSy2 and QSO2 at threshold $IO3 = 8.3$. The results are shown in Fig. 4 (right).

A clear dependence of the galaxy properties on AGN power is revealed. While bulge-dominated systems spread

Parametric Class	AGN type	With PS	Without PS
Bulge-dominated	HLSy2	(6/10) 60% $^{+4}_{-24}$	(4/5) 80% $^{+1}_{-35}$
	QSO2	(11/19) 58% $^{+5}_{-17}$	(7/8) 88% $^{+1}_{-28}$
Disk-dominated	HLSy2	(3/10) 30% $^{+10}_{-14}$	(1/5) 20% $^{+20}_{-10}$
	QSO2	(7/19) 37% $^{+12}_{-8}$	(1/8) 13% $^{+17}_{-6}$
PSF-dominated	HLSy2	(1/10) 10% $^{+14}_{-5}$	N/A
	QSO2	(1/19) 5% $^{+9}_{-2}$	N/A

Table 4. Comparison between the galaxy classification of HLSy2 and QSO2 with and without a point source. The fractions are quoted in brackets. Tentative evidence is hinted for a higher fraction of bulge-dominated systems in objects without a point source.

across the total range of $lO3$, disk-dominated galaxies concentrate mostly at $lO3 \lesssim 8.6$. This is in fact closer to the dividing luminosity $lO3=8.5$ between QSO2 and HLSy2 assumed by Zakamska et al. (2003) than to the 8.3 value assumed by Reyes et al. (2008). Considering the full sample, there are 10/36 or 28% $^{+8}_{-6}$ disk-dominated galaxies below $lO3=8.6$ and 2/21 or 10% $^{+10}_{-3}$ above.

The differentiation is even clearer when highly-disturbed systems are excluded. 38% $^{+10}_{-8}$ objects with $lO3 < 8.6$ are disk-dominated versus 13% $^{+14}_{-5}$ above this luminosity. There are 56% $^{+9}_{-10}$ bulge-dominated galaxies at $lO3 < 8.6$ and 87% $^{+5}_{-14}$ at $lO3 > 8.6$.

The increasing incidence of bulge-dominated systems with AGN luminosity is also apparent when we study the variation with $lO3$ of the relative contribution of the spheroidal-component to the total galaxy light (B/T) for the objects that could be fitted with GALFIT (Fig. 5). The average B/T increases with AGN power. Most objects with $lO3 \gtrsim 8.6$ have $B/T \gtrsim 70\%$, while at lower luminosities, the galaxies span the full range of possible B/T values.

4.4 Contribution from a point source

A point source has been isolated in 29 of the 42 objects (69% $^{+7}_{-8}$) for which the parametric method could be applied. The relative contribution to the total light of the galaxy in this subsample is in the range Light Fraction ($L.F.$) $\sim 3-51\%$ with median value 14.2% and standard deviation 14.8%. Even when $L.F.$ is small (\sim few%), this cannot be ignored in the fits, since the structural parameters of the hosts can be severely affected.

Our results are in good agreement with Inskip et al. (2010) (see Appendix B for a description of their sample). They found that the K-band images of 17 narrow line radio galaxies (NLRG) are often contaminated by a point source. They identified this component in 12 objects with $L.F.$ in the range $\sim 1-36\%$, and with median and standard deviation values 11.0% and 10.9% respectively.

This unresolved component is a combination of different sources whose relative contribution changes with spectral range. While in Inskip et al. (2010) an enhanced contribution of the AGN direct light may play a role due to less severe extinction effects in the near infrared, in our data the contamination by strong emission lines emitted by the compact narrow line region (NLR) is possibly high in many objects (see Table 1). Compact continuum sources are also

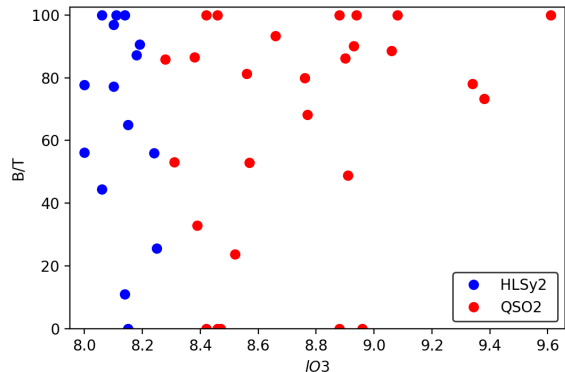


Figure 5. Relative contribution of the spheroidal-component to the total galaxy light (B/T) vs. $lO3$. Only galaxies that could be fitted with GALFIT are plotted. B/T increases with AGN power. For $lO3 \gtrsim 8.6$, most galaxies are bulge-dominated.

potential contributors such as nebular continuum associated with the NLR, scattered AGN light and nuclear starbursts (Dickson et al. 1995, Bruce et al. 2015, Bessiere et al. 2017).

We have compared the galaxy host classification for objects with and without point source (Table 4). The statistics is very poor and the errors large, so that significant differences cannot be claimed. On the other hand, tentative evidence is hinted for a higher fraction of bulge-dominated systems among objects (both QSO2 and HLSy2) with a point source.

We cannot discard that this is an artificial effect. We may be missing a point source in some objects, where this contribution cannot be clearly recognized by our fitting method. Ignoring the point source would result on steeper Sérsic profiles (and, thus, higher n values) for the central region of the galaxy hosts so that some may be miss-classified as bulge-dominated as a consequence. If this is the case, the fraction of bulge-dominated systems in galaxies with no point source would represent an upper limit.

The other alternative is that there is a real intrinsic difference between both groups (with and without point source contribution). Understanding the physical origin of such difference, if confirmed, would be of great interest possibly pointing to differences in opening angle of the central obscuring structure and/or the amount of obscuring dust in the central regions and/or orientation.

4.5 Kormendy relation

We show in Fig. 6 the Kormendy relation for our sample of host galaxies (Hamabe & Kormendy 1987). The effective radius, r_e , and the surface brightness magnitude at r_e , $\mu(r_e)$, are plotted only for the spheroidal component of galaxies. Errors on r_e are expected to be typically $\sim 10\%$ (Buitrago et al. 2018). We have assumed $\Delta\mu_e=0.5$ magnitude errors on $\mu(r_e)$. This is based on the study of how μ_e varies for a 10% change in r_e using different Sérsic profiles. This variation, $\Delta\mu_e$, is clearly larger in steeper (high n) profiles and it can be up to ~ 0.5 mag. This is the error we have used which is therefore conservative.

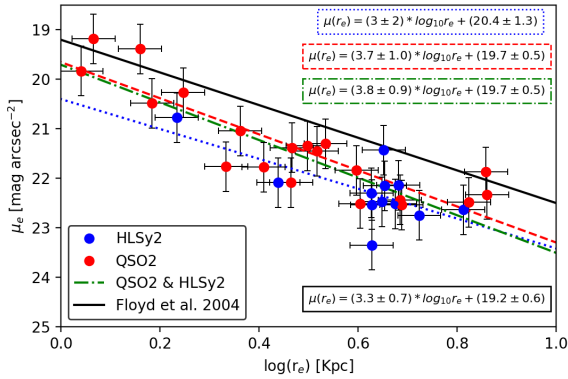


Figure 6. Relation between surface magnitude and effective radius for the spheroidal galaxies and bulges in our sample of luminous AGN. The best fits are shown for the QSO2, the HLSy2 and both groups together. The slope is consistent with that found by Floyd et al. (2004) for the bulge-dominated hosts of a sample of 14 QSO1 at $z \sim 0.4$.

The following relations are found:

$$\text{HLSy2} : \mu(r_e) = (3.0 \pm 2.0) \times \log(r_e) + (20.4 \pm 1.3)$$

$$\text{QSO2} : \mu(r_e) = (3.7 \pm 1.0) \times \log(r_e) + (19.7 \pm 0.5)$$

$$\text{HLSy2} + \text{QSO2} : \mu(r_e) = (3.8 \pm 0.9) \times \log(r_e) + (19.7 \pm 0.5)$$

The three trends have correlation coefficients $\rho^2 = 0.46, 0.76$ and 0.71 respectively (the weak trend for HLSy2 is biased by the outlying measurement of the more compact system with $\log(r_e) \sim 0.2$ kpc).

These relations are consistent within the errors with the scaling relation found by Bernardi et al. (2003) for 9000 SDSS early-type galaxies at $0.01 \leq z \leq 0.3$ (slope 3.33 ± 0.09).

It is also consistent with the relation found for the bulge-dominated host galaxies in Floyd et al. (2004) sample of QSO1 at $z \sim 0.4$ (Appendix B for a description of their sample; see also Dunlop et al. 2003).

$$\mu(r_e) = (3.3 \pm 0.7) \times \log(r_e) + (19.2 \pm 0.6)$$

Our sample is shifted down the vertical axis by ~ 0.6 magnitudes with respect to Floyd et al. (2004) QSO1, although the two samples are within the scatter both have ($\Delta\mu_e \sim \pm 0.6$). Both samples are basically at identical z , and thus redshift dimming does not play a role. We do not believe it is a consequence of the filters used either: 10 of 17 objects of Floyd et al. (2004) were observed with the same filter F814W as the majority of our sample. The other 7 were observed with the F791W filter, redder and slightly narrower. Several objects in our sample were observed with the ACS and with a significantly narrower filter than F814W. These objects are not shifted in any sense relative to the rest of the objects. The filters, therefore, do not seem to have any influence. Another possible effect is that Floyd et al. (2004) plot μ_e and r_e of the galaxies, and not only the spheroids, as we have done. Although all are bulge dominated, not removing the contribution of a disk may result on brighter

magnitudes. A final possibility is that the QSO1 are hosted by more luminous and more massive spheroids (see below).

The average $\langle r_e \rangle$ of the *spheroidal component* are 3.4 ± 0.5 kpc (median 3.0 ± 1.2 kpc) and 4.3 ± 0.4 kpc (median 4.5 ± 0.3 kpc) for QSO2 and HLSy2 respectively. For comparison Greene et al. (2009) obtain $\langle r_e \rangle = 3.1 \pm 0.8$ kpc (median 2.6 ± 0.5 kpc) for their sample of luminous QSO2 (Appendix B)³. These results tentatively suggest that QSO2 may be hosted by smaller spheroids than HLSy2. The uncertainties due to the poor statistics are however too large to confirm this.

We have also measured r_e for the total galaxies (spheroidal + disk components when present), excluding the point source, which can result on an underestimation of r_e even when the flux contribution is low ($< 10\%$)⁴. We obtain $\langle r_e \rangle = 3.9 \pm 0.6$ kpc (median 3.3 ± 1.6 kpc) for QSO2 and 5.0 ± 1.5 kpc (median 4.8 ± 0.9 kpc) for HLSy2.

The QSO2 sizes are significantly smaller than those measured for QSO1 and NLRG at similar z by other authors⁵. Inskip et al. (2010) sample of NLRG have $\langle r_e \rangle = 10.1 \pm 1.6$ kpc (median 10.0 kpc). Dunlop et al. (2003) radio-quiet and radio-loud QSO1 have $\langle r_e \rangle = 7.6 \pm 1.2$ kpc (median 6.4 kpc) and $\langle r_e \rangle = 8.2 \pm 0.8$ kpc (median 8.0 kpc) respectively. Floyd et al. (2004) obtain $\langle r_e \rangle = 7.2 \pm 1.3$ kpc and 6.1 ± 1.3 kpc for radio-loud and radio-quiet QSO1 respectively. Finally, $\langle r_e \rangle = 7.7 \pm 3.6$ kpc for Falomo et al. (2014) QSO1 sample.

Shen et al. (2003) found that early type galaxies ($n > 2.5$) at $z \sim 0$ with $\log(M_*/M_\odot)$ in the range 10.0-11.0 have $r_e \sim 2.1$ -4.2 kpc. Only galaxies with $\log(M_*) \gtrsim 11.4$ have sizes > 7 kpc. Wylezalek et al. (2016) inferred $\log(M_*/M_\odot) = 9.8$ -11.0 for a sample of 20 QSO2 at similar z as our sample, with median and average values 10.4 and 10.5 respectively⁶.

Therefore, the $\langle r_e \rangle$ we obtain for our QSO2 are in reasonable agreement with those expected based on the typical stellar masses inferred for other luminous QSO2. It is possible that the QSO1 and NLRG samples mentioned above are hosted by more massive galaxies.

5 DISCUSSION

Studies of low z QSO1 ($z \lesssim 0.5$) since the era of HST show that luminous quasars (radio-loud and radio-quiet) are hosted by a diversity of host galaxies, including ellipticals as bright as the brightest cluster ellipticals, normal ellipticals, spirals and highly-disturbed interacting systems (e.g. Bahcall et al. 1997, Kukula et al. 2001, Dunlop et al. 2003, Percival et al. 2001, Floyd et al. 2004, Falomo et al. 2014).

³ These values may be somewhat underestimated since the contribution of a point source is not taken into account

⁴ For comparison, if we do not take into account the contamination by the point source in our sample, $\langle r_e \rangle$ is 3.5 ± 0.6 for QSO2 and 4.5 ± 0.3 kpc for HLSy2 versus $\langle r_e \rangle = 3.9 \pm 0.6$ kpc and 5.0 ± 1.5 kpc respectively

⁵ For this comparison, we have converted all r_e values in other works to the Cosmology used by us

⁶ We have scaled their M_* to a Kroupa (2001) Initial Mass Function for comparison with Shen et al. (2003)

SDSS Name [1]	Method GALFIT [2]	Total		Point Source		1st Profile Component						2nd Profile Component					
		Mag (mag) [3]	R_{eff} (kpc) [4]	Mag (mag) [5]	Light Fraction [6]	Mag (mag) [7]	Light Fraction [8]	R_{eff} (kpc) [9]	n [10]	b/a [11]	PA ($^{\circ}$) [12]	Mag (mag) [13]	Light Fraction [14]	R_{eff} (kpc) [15]	n [16]	b/a [17]	PA ($^{\circ}$) [18]
J005515.82-004648.6	2B	19.3	1.5	20.4	35.00	19.7	65.00	2.4	1.2	0.57	68.5						
J011429.61+000036.7	2B	17.5	5.9	21.3	6.70	18.2	93.30	13.0	4.0	0.74	-58.7						
J011522.19+001518.5	1	18.1	4.5			18.1	100.00	6.3	4.0	0.59	-52.8						
J014237.49+144117.9	2B	17.8	1.1	20.4	20.00	18.8	80.00	1.5	4.0	0.75	-52.4						
J015911.66+143922.5	2B	19.5	1.2	22.1	18.67	20.4	81.33	1.9	1.4	0.81	-46.4						
J020234.56-093921.9	2A	17.6	6.3			18.7	32.97	2.4	4.0	0.81	-78.8	18.0	67.03	8.8	1.0	0.85	-81.3
J021059.66-011145.5	2B	19.0	3.0	20.7	22.80	19.2	77.20	8.2	2.5	0.48	69.9						
J023411.77-074538.4	2D	18.7	2.3	22.0	10.38	19.8	68.29	2.5	2.8	0.86	81.5	21.2	21.32	4.2	0.3	0.85	64.0
J031946.03-001629.1	2D	18.8	7.5			19.1	56.00	7.5	5.4	0.51	-63.3	19.7	44.00	8.9	0.3	0.80	-82.5
J031927.22+000014.5	1	18.8	4.5			18.7	100.00	7.4	3.8	0.64	33.8						
J032029.78+003153.5	2C	17.0	12.8	21.6	2.99	19.3	23.71	3.4	4.0	0.85	63.9	17.8	73.3	28.9	1.0	0.51	72.7
J034215.08+001010.6	1	19.2	1.1			19.1	100.00	0.7	6.0	0.82	-14.7						
J040152.38-053228.7	2B	19.0	2.7	21.1	12.17	18.9	87.83	2.9	1.0	0.87	-40.1						
J074811.44+395238.0	2B	18.7	4.6	21.3	9.45	18.6	90.55	9.4	4.0	0.89	-70.5						
J081125.81+073235.3	1	19.2	4.0			19.2	100.00	5.9	4.2	0.73	-0.9						
J082449.27+370355.7	2B	19.0	1.3	21.1	14.20	19.1	85.80	2.0	5.7	0.72	62.5						
J082527.50+202543.4	2B	19.7	1.1	20.4	49.48	20.4	50.52	1.5	1.0	0.95	-64.5						
J083028.14+202015.7	2C	18.5	2.5	20.8	11.85	19.2	48.83	1.8	4.0	0.33	-38.6	19.4	39.32	3.1	1.0	0.95	11.2
J084041.08+383819.8	2C	17.8	7.1	20.8	6.46	19.7	18.47	4.2	0.4	0.33	5.2	18.1	75.08	9.5	1.0	0.81	-28.3
J084309.86+294404.7	2B	18.7	3.1	20.3	22.02	19.0	77.98	6.7	2.6	0.87	-49.0						
J084856.58+013647.8	1	17.1	4.9			17.9	100.00	18.7	5.0	0.87	-39.6						
J084943.82+015058.2	2C	19.5	2.2	21.2	21.57	20.2	44.41	3.8	4.0	0.41	66.4	20.7	34.03	3.1	1.0	0.47	50.8
J090414.10-002144.9	2B	17.8	2.9	21.3	9.90	18.3	90.10	9.6	6.5	0.52	-67.3						
J092318.06+010144.8	1	18.8	3.1			18.8	100.00	4.1	4.0	0.68	-46.5						
J094209.00+570019.7	2D	18.7	1.6	19.9	31.42	19.4	53.12	4.3	5.2	0.91	-54.4	20.7	15.46	4.3	0.2	0.75	-86.3
J094350.92+610255.9	2B	19.6	1.0	20.2	49.77	20.3	50.23	1.4	1.0	0.85	-48.1						
J095629.06+573508.9	2B	19.0	3.2	21.3	13.44	19.1	86.56	4.5	2.2	0.58	-80.5						
J100329.86+511630.7	1	18.4	4.8			18.4	100.00	6.3	2.5	0.48	75.8						
J103639.39+640924.7	1	17.8	7.3			17.8	100.00	14.0	4.0	0.65	19.6						
J112907.09+575605.4	2D	19.1	2.4	21.8	9.38	19.2	73.34	5.1	4.0	0.70	-5.2	21.0	17.28	1.8	0.2	0.07	-7.6
J113710.78+573158.7	1	18.6	3.3			18.6	100.00	7.5	6.5	0.53	-48.3						
J140740.06+021748.3	2D	19.2	1.5			19.3	86.28	1.2	5.6	0.46	-45.3	21.2	13.72	5.2	0.5	0.15	-35.8
J150117.96+545518.3	2B	17.2	6.1	19.5	11.39	17.2	88.61	8.5	2.3	0.88	62.3						
J154133.19+521200.1	2A	18.0	6.7			19.5	25.59	2.0	4.6	0.65	-29.7	18.1	74.41	9.8	1.0	0.79	-19.7
J154613.27-000513.5	2B	19.0	3.8	21.3	12.71	19.1	87.29	5.9	2.4	0.84	-51.2						
J172419.89+551058.8	2B	19.3	1.4	20.3	43.86	19.9	56.14	5.0	1.7	0.63	63.9						
J172603.09+602115.7	2B	19.8	1.2	20.6	47.06	20.3	52.94	2.6	1.4	0.52	45.4						
J173938.64+544208.6	2C	19.2	2.6	20.9	20.51	20.3	35.77	1.9	0.8	0.54	37.9	20.1	43.72	8.5	1.0	0.51	33.4
J214415.61+125503.0	2C	18.5	1.2	19.0	50.67	19.8	11.05	16.6	5.4	0.32	-32.9	19.2	38.29	5.1	1.0	0.73	-72.2
J223959.04+005138.3	2C	18.9	3.6	20.5	22.12	20.7	19.38	2.1	0.3	0.74	-1.8	19.2	58.50	9.3	1.0	0.50	61.8
J231755.35+145349.4	2B	18.3	6.2	22.1	3.10	18.3	96.90	9.7	2.0	0.60	79.1						
J231845.12-002951.4	2D	18.4	4.3	20.1	9.85	18.1	77.73	24.7	4.8	0.78	48.6	20.6	12.41	7.2	0.3	0.20	23.4

Table 5. List of the 42/57 objects that could be fitted with GALFIT and results of the best fits. Col(2): Method to obtain the best fit. 1: Single Sérsic, 2A:Sérsic+Disk, 2B: PS+Sérsic, 2C: PS+Disk+Sérsic, 2D:Other. Col(3,4): Total magnitude and effective radius R_{eff} in kpc of the GALFIT galaxy model. Col(5,6): Magnitude and relative contribution (light fraction) to the total galaxy luminosity of the point source. Col(7 to 12): Magnitude, light fraction and structural parameters of 1st component identified with GALFIT. Col(13 to 18): same for 2nd component. Sérsic index n , axis ratio b/a , position angle (east of north) PA .

Object SDSS [1]	<i>l</i> O3 [2]	This work			B/T Classification		Visual vs. Parametric [8]
		Vis-I [3]	Vis-II [4]	Vis-III [5]	Method [6]	Details [7]	
J002531.46-104022.2	8.73	HD	1	2N, T, K?	N/A	HD	
J005515.82-004648.6	8.15	El	0		2B	Disk-Dominated	El vs. Disk-Dominated
J011429.61+000036.7	8.66	El	0	PC	2B	Bulge-Dominated	
J011522.19+001518.5	8.14	El	0*	A, tt, PC	1	Bulge-Dominated	
J014237.49+144117.9	8.76	El	0*	PC, S,D, tt, K?	2B	Bulge-Dominated	
J015911.66+143922.5	8.56	El	0		2B	Disk-Dominated	El vs. Disk-Dominated
J020234.56-093921.9	8.39	Sp	1	IC,B, K?	2A	Disk-Dominated	
J021059.66-011145.5	8.10	Sp	0*	S	2B	Bulge-Dominated	Sp vs. Bulge-Dominated
J021758.18-001302.7	8.55	HD	2	T,D	N/A	HD	
J021834.42-004610.3	8.85	HD	1	T,C,IC = 2N	N/A	HD	
J022701.23+010712.3	8.90	HD	2	2 N, T, D, S , A	N/A	HD	
J023411.77-074538.4	8.77	El	0		2D	Bulge-Dominated	
J031946.03-001629.1	8.24	Sp or Disk	0		2D	Bulge-Dominated	Sp or Disk vs. Bulge-Dominated
J031927.22+000014.5	8.06	El	0*	F, tt?	1	Bulge-Dominated	
J032029.78+003153.5	8.52	El	0*	D, PC	2C	Disk-Dominated	El vs. Disk-Dominated
J032533.33-003216.5	9.06	El	2	T	N/A	HD	El vs. HD
J033310.10+000849.1	8.13	HD	1	2N/D?, T, K?, IC	N/A	HD	
J034215.08+001010.6	9.08	El	0		1	Bulge-Dominated	
J040152.38-053228.7	8.96	El	0*	A, PC?	2B	Disk-Dominated	El vs. Disk-Dominated
J074811.44+395238.0	8.19	El	2	T, K?	2B	Bulge-Dominated	
J081125.81+073235.3	8.88	El	0*	A, IC?, I	1	Bulge-Dominated	
J081330.42+320506.0	8.83	El?	2	T,tt, D, I, A	N/A	HD	El? vs. HD
J082449.27+370355.7	8.28	El	0		2B	Bulge-Dominated	
J082527.50+202543.4	8.88	El	0		2B	Disk-Dominated	El vs. Disk-Dominated
J083028.14+202015.7	8.91	El	0		2C	Bulge-Dominated	
J084041.08+383819.8	8.47	Sp	2	T, K?	2C	Disk-Dominated	
J084309.86+294404.7	9.34	El	0		2B	Bulge-Dominated	
J084856.58+013647.8	8.46	El	0*	S, A, PC	1	Bulge-Dominated	

Table 6. Results of the visual and parametric classification (see Section 3 for details): Col(3) indicates the galaxy morphological type based on Method Vis-I: El (elliptical), Sp (spiral), Disk (disk galaxy with no obvious spiral arms), HD (highly-disturbed: when 2 or more components are interacting and make the classification in the previous groups difficult). Col(4): type of merger based on Method Vis-II following Rodríguez Zaurín et al. (2011) and Veilleux et al. (2002): 0= Isolated undisturbed galaxy, 0*= Isolated disturbed galaxy, 1= two nuclei with projected separation > 1.5 kpc; 2 = two nuclei with projected separation ≤ 1.5 or single nucleus with signatures of a post-coalescence phase. Col(5) specify the nature of the peculiar features based on Method Vis-III following Ramos-Almeida et al. (2011). T: Tidal tail; F: Fan; B: Bridge; S: Shell; D: Dust feature; 2N: Double Nucleus; A: Amorphous Halo; I: Irregular feature. IC: interacting companion. Other features we include in this work are 2N*: two nuclei with relative distance greater than 1.5 kpc, PC: projected companion, this is, there is an object close to the target in projection with no clear physical relation, K: Knot, tt: Streams. A question mark "?" indicates uncertain classification or identification. Col(6): classification based on the parametric method (Table 5). N/A refers to objects that could not be fitted with GALFIT. Col(7): type of profile according to the dominant structural component: HD in this column are highly-disturbed objects that could not be fitted with GALFIT. The vast majority are highly-disturbed systems. Point source: system dominated by a spatially unresolved source; Disk-dominated: system dominated by a disk or disk-like component; Bulge-dominated: system dominated by a spheroidal component. Col(8): Comparison between the visual and parametric classifications.

Object SDSS [1]	$lO3$ [2]	This work			B/T Classification		Visual vs. Parametric [8]
		Vis-I [3]	Vis-II [4]	Vis-III [5]	Method [6]	Details [7]	
J084943.82+015058.2	8.06	El	0		2C	Bulge-Dominated	
J090307.84+021152.2	8.42	HD	1/2	2N*, T, K, D	N/A	HD	
J090414.10-002144.9	8.93	El	2	T, F	2B	Bulge-Dominated	
J090801.32+434722.6	8.31	El	2	T, I, K	N/A	HD	El vs. HD
J092318.06+010144.8	8.94	Sp	0*	T?	1	Bulge-Dominated	Sp vs B
J092356.44+012002.1	8.59	El	1/2	T	N/A	HD	El vs. HD
J094209.00+570019.7	8.31	El	1	T, D, F, tt, PC	2D	Bulge-Dominated	
J094350.92+610255.9	8.46	El	0		2B	Point Source	El vs. Point Source
J095629.06+573508.9	8.38	El	0		2B	Bulge-Dominated	
J100329.86+511630.7	8.11	El	2	T, A, F	1	Bulge-Dominated	
J103639.39+640924.7	8.42	El	2	T, PC	1	Bulge-Dominated	
J112907.09+575605.4	9.38	El	0*	I	2D	Bulge-Dominated	
J113710.78+573158.7	9.61	El	0*	T, tt	1	Bulge-Dominated	
J133735.01-012815.7	8.72	El	2	T?, 2N, I	N/A	HD	El vs. HD
J140740.06+021748.3	8.90	Sp or Disk	0		2D	Bulge-Dominated	Sp or Disk vs. Bulge-Dominated
J143027.66-0056149	8.44	HD	1	2N, T, IC?, K, A	N/A	HD	
J144711.29+021136.2	8.45	HD	1/2	2N*, T, B	N/A	HD	
J150117.96+545518.3	9.06	El?	1	IC, S,D, T, B, K?	2B	Bulge-Dominated	
J154133.19+521200.1	8.25	Sp	2	S, K, T, IC?	2A	Disk-Dominated	
J154337.81-004420.0	8.40	HD	1	2N, T,F,I, A	N/A	HD	
J154613.27-000513.5	8.18	El	0		2B	Bulge-Dominated	
J172419.89+551058.8	8.00	El	0		2B	Disk-Dominated	El vs. D
J172603.09+602115.7	8.57	El	0		2B	Disk-Dominated	El vs. Disk-Dominated
J173938.64+544208.6	8.42	Sp or Disk	0*	tt?	2C	Disk-Dominated	
J214415.61+125503.0	8.14	El	2	I,T	2C	Point Source	El vs. Point Source
J215731.40+003757.1	8.39	HD	1	D,IC	N/A	HD	
J223959.04+005138.3	8.15	Sp or Disk	0*	A?	2C	Disk-Dominated	
J231755.35+145349.4	8.10	Sp	0	C	2B	Bulge-Dominated	Sp vs. Bulge-Dominated
J231845.12-002951.4	8.00	Sp	0		2D	Bulge-Dominated	Sp vs. Bulge-Dominated

Table 6. (Cont.)

Some of these works have suggested that the type of galaxy host depends on AGN power, so that the most luminous AGN (quasars) tend to be hosted by massive ellipticals (Dunlop et al. 2003, Floyd et al. 2004). This is however controversial and other works claim a higher incidence of galaxies with disks in luminous quasars (e.g. Cales et al. 2011, Falomo et al. 2014).

The contribution of this work to the topic of the host galaxies associated with quasars is based on: 1) due to their recent discovery, just a few studies exist (two, to the best of our knowledge: Greene et al. 2009, Wylezalek et al. 2016) regarding the structural properties of $z < 1$ QSO2 host galaxies. They have been focussed on samples of up to ~ 20 objects. We expand these works with 41 more QSO2 and complement it with 16 HLSy2; 2) we take into account factors that sometimes have not been considered, such as the high incidence of highly-disturbed systems, the contribution of a point source and/or the presence of several structural components in galaxies; 3) we perform a thorough comparative study with related parametric works of the host galaxies of luminous AGN at similar z (see Sect. 5.1).

Our analysis has shown a wide diversity of galaxy hosts among both HLSy2 and QSO2 (Tables 7 and 8). An interesting result is that a high fraction ($\sim 55\%$) of QSO2 are *not* hosted by bulge-dominated galaxies. Although these are the most numerous group ($44\%_{-10}^{+5}$), more than half QSO2 are hosted by other galaxy types, mostly highly-disturbed systems due to galaxy interactions ($34\%_{-9}^{+6}$) and disk-dominated systems ($20\%_{-6}^{+6}$). The main difference between QSO2 and HLSy2 is the lower incidence of morphologically-disturbed systems among HLSy2 ($6\%_{-3}^{+10}$). This is consistent with a scenario in which galaxy interactions are the dominant mechanism triggering the activity at the highest AGN power (e.g. Hopkins et al. 2008; Bessiere et al. 2012; Ramos-Almeida et al. 2011).

Although disks are identified in $44\%_{-11}^{+13}$ of HLSy2 and $24\%_{-6}^{+8}$ QSO2, disk-dominated systems represent a minority ($25\%_{-11}^{+8}$ HLSy2 and $20\%_{-6}^{+6}$ QSO2). Excluding highly-disturbed systems, if we consider the coarse division QSO2 vs. HLSy2 at $IO3 = 8.3$, both groups show a similar distribution among galaxy types (Tables 7 and 8). However, a more careful analysis reveals that the galaxy properties do change with AGN power: the relative contribution of the spheroidal component to the total galaxy light (B/T) increases with $IO3$ (Sec. 4.3). Excluding the complex merger/interaction systems, $B/T \gtrsim 0.7$ for most galaxies with $IO3 \gtrsim 8.6$. As other authors have argued, this is naturally expected if more powerful AGN are powered by more massive black holes which in turn are hosted by more massive bulges or spheroids (Magorrian et al. 1998, Dunlop et al. 2003). Constraining the galaxy masses of the sample studied here would very valuable to investigate this scenario.

5.1 Comparison with other works

We put the results of our parametric analysis in the context of other relevant works. We focus our comparison on the QSO2 sub-sample and related studies of AGN with quasar like luminosities (QSO1, QSO2 and NLRG). While

our HLSy2 are at the high end of Sy2 luminosities, related studies on Seyferts cover a much wider range usually extending to significantly lower AGN power, so that the comparison is not trivial (Kauffmann et al. 2003).

We also focus on studies based on samples at $z \lesssim 0.5$. The comparison with high z studies is complicated by the limited physical spatial information and/or the shallowness of the data and/or the different rest-frame spectral range (e.g. rest-frame UV at $z > 2$ versus rest-frame optical at low z). Detailed information on all referenced works can be found in Appendix B.

Firm conclusions regarding the origin of some discrepancies and similarities between works are not possible due to the numerous potential influencing factors on the galaxy classification: poor statistics, data properties (depth, spectral range, spatial resolution), sample selection (range of AGN luminosities, radio-loudness, obscured versus unobscured), fitting method (e.g. one versus several structural components; classification criteria based on n values). For the sake of clarity, we mention for each work the available information that can help the reader identify the possible influencing factors (Appendix B). The results of all works are summarized in Tables 7 and 8. The confidence intervals have been calculated as in Sect. 4.1.1.

In spite of the above limitations, some interesting results appear, which can be summarized as follows.

- A clear difference between works is the incidence of highly-disturbed merger/interaction systems, which are absent in several works while they account for $\sim 34\%$ of our QSO2 sample. The reason for the discrepancy lies, at least in part, in that the classification and/or fitting methods are often not sensitive to the distinction of such systems.

- In general, all works are consistent regarding the fraction of disk-dominated galaxies ($\sim 10\text{-}20\%$) and B+D systems (\lesssim few %) in radio-quiet quasars. This fraction is tentatively lower in radio-loud QSO1 and NLRG ($\lesssim 6\%$, Dunlop et al. 2003; Inskip et al. 2010). This is consistent with the fact that powerful radio-loud objects tend to be hosted by massive elliptical galaxies (Matthews et al. 1964; Best et al. 2005).

Falomo et al. (2014) is an exception. They find a significantly higher fraction of disk-dominated systems ($42\%_{-3}^{+3}$) and B+D ($21\%_{-3}^{+3}$). They identify disks in a high fraction of quasars $\sim 63\%$ (e.g. $\sim 24\%$ in our sample). A real difference in the type of galaxy hosts cannot be discarded, but it must be kept in mind that the fitting and classification method applied are, as the authors warn, too simplistic and can only yield a preliminary indication of the morphology (Appendix B).

- All works are consistent in that the most numerous group of host galaxies are always bulge-dominated (Falomo et al. 2014 is again an exception). On the other hand, the percentage varies significantly. In general, studies that do not separate complex merger/interaction systems (Dunlop et al. 2003; Floyd et al. 2004; Inskip et al. 2010; Wylezalek et al. 2016) result on a higher fraction of bulge-dominated galaxies ($\sim 76\text{-}100\%$) compared with other works where disturbed systems are identified ($44\text{-}62\%$, our work, Greene et al. 2009; Cales et al. 2011). Thus, the classification criteria may play a role on the observed differences.

Moreover, intrinsic differences between samples proba-

	Disk-dominated	Bulge-dominated	B+D*	Point Source	Disturbed
This work (HLSy2)	25% $^{+8}_{-11}$	63% $^{+1}_{-21}$	0% $^{+9}$	6% $^{+10}_{-3}$	6% $^{+10}_{-3}$
This work (QSO2)	20% $^{+6}_{-6}$	44% $^{+5}_{-10}$	0% $^{+4}$	2% $^{+5}_{-0.9}$	34% $^{+6}_{-9}$
Dunlop et al. (2003) (RL-QSO1)		100% $_{-16}$			
Dunlop et al. (2003) (RQ-QSO1)	15% $^{+15}_{-6}$	85% $^{+6}_{-15}$			
Floyd et al. (2004) (QSO1)	18% $^{+11}_{-7}$	76% $^{+8}_{-13}$	6% $^{+11}_{-3}$		
Falomo et al. (2014) (QSO1)	42% $^{+3}_{-3}$	37% $^{+3}_{-3}$	21% $^{+3}_{-3}$		
Cales et al. (2011) (QSO1)	21% $^{+8}_{-7}$	62% $^{+4}_{-14}$	3% $^{+7}_{-1.2}$		14% $^{+8}_{-5}$
Greene et al. (2009) (QSO2)	20% $^{+12}_{-8}$	53% $^{+9}_{-16}$			27% $^{+12}_{-10}$
Wylezalek et al. (2016) (QSO2)	10% $^{+11}_{-4}$	90% $^{+4}_{-11}$			
Inskip et al. (2010) (NLRG)	6% $^{+11}_{-3}$	88% $^{+1}_{-17}$	6% $^{+11}_{-3}$		

Table 7. Comparison with other works. *B/D include intermediate classification in works that use only one Sérsic profile and n has an intermediate value between disk-dominated and bulge-dominated objects assumed by the authors.

	Disk-dominated	Bulge-dominated	B+D*
This work (HLSy2)	29% $^{+12}_{-10}$	71% $^{+5}_{-19}$	0% $^{+11}$
This work (QSO2)	31% $^{+9}_{-9}$	69% $^{+6}_{-13}$	0% $^{+7}$
Dunlop et al. (2003) (RL-QSO1)		100% $_{-16}$	
Dunlop et al. (2003) (RQ-QSO1)	15% $^{+15}_{-6}$	85% $^{+6}_{-15}$	
Floyd et al. (2004) (QSO1)	18% $^{+11}_{-7}$	76% $^{+8}_{-13}$	6% $^{+11}_{-3}$
Falomo et al. (2014) (QSO1)	42% $^{+3}_{-3}$	37% $^{+3}_{-3}$	21% $^{+3}_{-3}$
Cales et al. (2011) (QSO1)	24% $^{+9}_{-7}$	72% $^{+5}_{-13}$	4% $^{+8}_{-1.4}$
Greene et al. (2009) (QSO2)	27% $^{+19}_{-9}$	73% $^{+9}_{-17}$	
Wylezalek et al. (2016) (QSO2)	10% $^{+11}_{-4}$	90% $^{+4}_{-11}$	
Inskip et al. (2010) (NLRG)	6% $^{+11}_{-3}$	88% $^{+1}_{-17}$	6% $^{+11}_{-3}$

Table 8. As Table 6 but excluding highly-disturbed systems.

bly also play a role. For instance, the radio-loud (Dunlop et al. 2003; Inskip et al. 2010) and most luminous samples (Wylezalek et al. 2016) show tentative evidence for the highest fraction of bulge-dominated systems. This is naturally expected. On one hand, radio loudness is favoured in massive bulge dominated galaxies, as mentioned above. On the other hand, as we have seen, the relative contribution of the spheroidal component to the total galaxy light increases with $lO3$, proxy of AGN power (Sect. 4.3).

6 SUMMARY AND CONCLUSIONS

We have studied the morphological and parametric properties of the host galaxies of 57 optically-selected luminous type 2 AGN at $0.3 \lesssim z \lesssim 0.4$ from the SDSS. The sample consists of 41 QSO2 with $8.31 \leq lO3 \leq 9.61$ and 16 high-luminosity Seyfert 2 (HLSy2) with $8.06 \leq lO3 \leq 8.28$. Our study is based on HLA archive ACS/WFC and WFPC2 HST

images. Both samples contain $\sim 44\%$ of all SDSS optically selected QSO2 and HLSy2 within the same z and $L_{[OIII]}$ ranges. Although uncertainties remain regarding the exact selection criteria, we consider them an adequate representation of the original total SDSS samples.

Due to the recent discovery of QSO2 in large numbers, the structural properties of their host galaxies are poorly known. To our knowledge, only two related studies have been published for $z < 1$ QSO2, with 35 QSO2 hosts parametrized so far (Greene et al. 2009, Wylezalek et al. 2016). Our work expands this investigation with 41 more QSO2 and complements it with 16 HLSy2.

We have classified the galaxies both visually and, most importantly, parametrically using the code GALFIT. The parametric analysis is essential to isolate and parametrize the individual structural galactic components and, ultimately, classify the galaxies in terms of the dominant component.

The main results and conclusions of our study are:

- There is a wide diversity of galaxy hosts among both HLSy2 and QSO2. Less than half ($44\%_{-10}^{+5}$) of QSO2 are hosted by bulge-dominated galaxies (in our terminology this includes spheroidal galaxies and galaxies with $B/D > 1.2$). More than half are hosted by other galaxy types, mostly highly-disturbed systems due to galaxy mergers/interactions ($34\%_{-9}^{+6}$) and disk-dominated systems ($20\%_{-6}^{+6}$, these are disk like galaxies and galaxies with $B/D < 0.8$). A minority of galaxies are dominated by a point source ($2\%_{-0.9}^{+5}$).

- Among HLSy2, $63\%_{-21}^{+1}$ are bulge-dominated, $25\%_{-11}^{+8}$ are disk-dominated and $6\%_{-3}^{+10}$ are highly-disturbed systems. $6\%_{-3}^{+10}$ are dominated by a point source.

- A significant difference between QSO2 and HLSy2 is the higher incidence of morphologically disturbed systems among QSO2 ($34\%_{-9}^{+6}$ versus $6\%_{-3}^{+10}$). This is consistent with a scenario in which galaxy interactions are the dominant mechanism triggering the activity at the highest AGN power.

- Disks are identified in a significantly higher fraction of HLSy2 ($44\%_{-11}^{+13}$) than QSO2 ($24\%_{-6}^{+8}$) but this is a result of the lower fraction of disturbed systems among Seyferts. When these are not considered, the fractions become consistent within the errors ($47\%_{-12}^{+13}$ HLSy2 and $37\%_{-8}^{+10}$ QSO2).

- The coarse and somewhat arbitrary division between HLSy2 and QSO2 at $IO3 = 8.3$ is not adequate to unveil trends of galaxy host with $IO3$ (used here as proxy of AGN power). A more detailed analysis using a finer sampling of $IO3$, reveals a clear dependence of the galaxy properties with AGN power. The relative contribution of the spheroidal component to the total galaxy light (B/T) increases with $L_{[OIII]}$. $B/T \gtrsim 0.7$ for most QSO2 with $IO3 \gtrsim 8.6$, while at lower luminosities the galaxies span the full range $B/T \sim 0.0-1.0$. While bulge-dominated systems spread across the total range of $L_{[OIII]}$ of the sample, most disk-dominated galaxies concentrate at $IO3 \lesssim 8.6$.

As other authors have argued, this is naturally expected if more powerful AGN are powered by more massive black holes which in turn are hosted by more massive bulges or spheroids. Constraining the galaxy masses of the sample studied here would be very valuable to investigate this scenario.

- A point source component is isolated in a high fraction of objects (10/16 or $63\%_{-13}^{+11}$ HLSy2 and 19/41 or $\sim 46\%_{-8}^{+8}$ QSO2), although it rarely dominates the total flux. The relative contribution to the total galaxy light is in the range $\sim 3-51\%$ (median value 14.2%). In spite of being obscured AGN, even when the light fraction is small (\sim few%), this point source cannot be ignored in the fits, since the structural parameters of the hosts can be severely affected.

- We have compared our results with other works dedicated to the parametric classification of the host galaxies of luminous AGN in the quasar regime (QSO, QSO2 and NLRG). All works are in general consistent regarding the fraction of disk-dominated galaxies in radio-quiet QSO1 and QSO2 ($\sim 10-20\%$). This fraction appears to be lower in radio-loud systems. This is consistent with the fact that powerful radio-loud AGN tend to be hosted by massive ellipticals. All works are in general also consistent in that bulge-dominated systems are the most numerous, although the percentages vary significantly among works. This is due to possible difference between samples (e.g. radio-loud versus radio-quiet, range of AGN power), differences in the parametric classifi-

cation method and the misclassification of highly-disturbed systems.

- The spheroidal component of the host galaxies of the sample studied here follows the Kormendy relation defined by early-type galaxies at $0.01 \leq z \leq 0.3$. The slope is also consistent with the relation found for the bulge-dominated host galaxies of QSO1 at similar z . The average galaxy sizes (correcting for PSF contamination) are $\langle r_e \rangle = 3.9 \pm 0.6$ kpc (median 3.3 ± 1.6 kpc) for QSO2 and 5.0 ± 1.5 kpc (median 4.8 ± 0.9 kpc) for HLSy2. The QSO2 sizes are consistent with those expected for non active galaxies at $z \sim 0$ of stellar masses in the range expected for our sample. They are, on the other hand, smaller than $\langle r_e \rangle \sim 7-10$ kpc quoted in the literature for QSO1 and NLRG. The latter samples may be biased towards more massive galaxies.

ACKNOWLEDGMENTS

Thanks to an anonymous referee for useful comments on and suggestions on the paper. JUM and MVM acknowledge support from the Spanish former Ministerio de Economía y Competitividad through the grants AYA2012-32295 and AYA2015-64346-C2-2-P. FB acknowledges the support by FCT via the postdoctoral fellowship SFRH/BPD/103958/2014. This work is supported by Fundacao para a Ciencia e a Tecnologia (FCT) through national funds (UID/FIS/04434/2013) and by FEDER through COMPETE2020 (POCI-01-0145-FEDER-007672). FB also acknowledges support from grant AYA2016-77237-C3-1-P from the Spanish Ministry of Economy and Competitiveness (MINECO). JPL acknowledges support from the Spanish Ministerio de Economía y Competitividad through the grant AYA2017-85170-R. BRP acknowledges financial support from the Spanish Ministry of Economy and Competitiveness through grant ESP2015-68964. F.J.C. acknowledges financial support through grant AYA2015-64346-C2-1-P (MINECO/FEDER).

We thank Enrica Bellocchi for useful scientific discussions and Boris Häussler and Chien Peng for valuable advice on the use of GALFIT.

Based on observations made with the NASA/ESA Hubble Space Telescope, and obtained from the Hubble Legacy Archive, which is a collaboration between the Space Telescope Science Institute (STScI/NASA), the Space Telescope European Coordinating Facility (ST-ECF/ESA) and the Canadian Astronomy Data Centre (CAD/C/NRC/CSA).

This research has made use of: 1) the VizieR catalogue access tool, CDS, Strasbourg, France. The original description of the VizieR service was published in Ochsenbein et al. 2000; 2) the NASA/IPAC circumgalactic Database (NED) which is operated by the Jet Propulsion Laboratory, California Institute of Technology, under contract with the National Aeronautics and Space Administration;

This research has made use of CosmoCalc Wright 2006 to obtain the scale kpc/" of each object. This research (to correct Galactic extinction) has made use of the NASA/IPAC Extragalactic Database (NED), which is operated by the Jet Propulsion Laboratory, California Institute of Technology, under contract with the National Aeronautics and Space Administration.

We have extensively used the following software pack-

ages: TOPCAT (Taylor 2005), IDL Astronomy Library (Landsman 1993), the Python routines of PyRAF and STSDAS (STSDAS and PyRAF are products of the Space Telescope Science Institute, which is operated by AURA for NASA) and Matplotlib (Hunter 2007). This research made use of Astropy, a community-developed core Python package for Astronomy (Astropy Collaboration, 2013).

REFERENCES

- Antonucci R., 1993, *ARA&A*, 31, 473
- Allen P. D., Driver S. P., Graham A. W., Cameron E., Liske J., De Propis R., 2006, *MNRAS*, 371, 2
- Bahcall J., Kirhakos S., Saxe D.H., Schneider D.P., 1997, *ApJ*, 479, 642
- Barentine J. C., Kormendy J., 2012, *ApJ*, 754, 140
- Bernardi M. et al. 2003, *ApJ*, 125, 1849
- Bessiere P. S., Tadhunter C. N., Ramos Almeida C., Villar Martín M., 2012, *MNRAS*, 426, 276
- Bessiere P. S., Tadhunter C. N., Ramos Almeida C., Villar Martín M., Cabrera-Lavers A., 2017, *MNRAS*, 466, 388
- Bertin E., Arnouts S., 1996, *A&A*, 117, 393
- Best P.N., Kauffmann G., Heckman T. M., Brinchmann J., Charlot S., Ivezić Z., White S. D. M., 2005, *MNRAS*, 362, 25
- Bettoni D., Falomo R., Kotilainen J. K., Karhunen K., Uslenghi M., 2015, *MNRAS*, 454, 4103
- Balcells M., Graham Alister W., Peletier R. F., 2007, *ApJ*, 665, 1084
- Bruce V. A., Dunlop J. S., Mortlock A., Kocevski D. D., McGrath E. J., Rosario D. J., 2015, *MNRAS*, 458, 2391
- Buitrago F., Trujillo I., Conselice C. J., Bouwens R. J., Dickinson M., Yan H., 2008, *ApJ*, 687, L61
- Buitrago F., Trujillo I., Conselice C. J., Häußler B., 2013, *MNRAS*, 428, 1460
- Buitrago F., Trujillo I., Curtis-Lake E., Montes M., Cooper A. P., Bruce V. A., Pérez-González P. G., Cirasuolo M., 2017, *MNRAS*, 466, 4888
- Buitrago F., Ferreras I., Kelvin L.S., 2018, *MNRAS*, in press (arXiv:1807.02534)
- Choi Y. Y., Woo J. H., Park C., 2009, *ApJ*, 699, 1679
- Cales S.L. et al., 2011, *ApJ*, 741, 106
- Cameron E., 2011, *PASA*, 28, 128
- Cisternas M. et al. 2011, *ApJ*, 726, 57
- Clopper C.J., Pearson E.S., 1934, *Biometrika*, 26, 404
- Combes F., 2001, in Aretxaga I., Kunth D., Mújica R., eds, *Advanced Lectures on the Starburst-AGN Connection, Fueling the AGN*. World Scientific, Singapore, p. 223
- Davari R., Ho L. C., Peng C. Y., 2016, *ApJ*, 824, 112
- de Vaucouleurs G., 1959, *Handbuch der Physik*, 53, 275
- Dickson R., Tadhunter C., Shaw M., Clark N., Morganti R., 1995, *MNRAS*, 273, 29
- Draper A. R., Ballantyne D. R., 2012, *ApJ*, 751, 72
- Dunlop J., McLure R., Kukula M., Baum S., O’Dea C., Hughes D.H., 2003, *MNRAS*, 340, 1095
- Faber S. M. et al., 1997, *ApJ*, 114, 1771
- Falomo R., Bettoni D., Karhunen K., Kotilainen J. K., Uslenghi M., 2014, *MNRAS*, 440, 276
- Fanti C., Fanti R., Lori C, Padrielli L., van der Laan H., de Ruiter H., 1977, *A&A*, 61, 487
- Ferrarese L. & Merritt D., 2000, *ApJ*, 539, L9
- Floyd D. J. E., Kukula M. J., Dunlop J. S., McLure R. J., Miller L., Percival W. J., Baum S. A., O’Dea C. P., 2004, *MNRAS*, 355, 196
- Floyd D. J. E., Dunlop J. S., Kukula M. J., Brown M. J. I., McLure R. J., Baum S. A., O’Dea C. P., 2013, *MNRAS*, 429, 2
- Freeman K. C., 1970, *ApJ*, 160, 811
- Gabor J. M. et al., 2009, *ApJ*, 691, 705
- Gadotti D. A., 2009, *MNRAS*, 393, 1531
- Gebhardt K. et al., 2000, *ApJ*, 539, 13
- Gilli R. et al., 2011, *MSAIS*, 17, 85
- Graham A. W., Driver S. P., Petrosian V., Conselice C. J., Bershadsky M. A., Crawford S. M., Goto T., 2005, *AJ*, 130, 1535
- Greene J. E., Zakamska N.L., Liu X., Barth A. J., Ho L. C., 2009, *ApJ*, 702, 441
- Hamabe M., Kormendy J., 1987, in *Structure and Dynamics of Elliptical Galaxies*, Proceedings of IAU Symp. No. 127, p. 279. Ed. T. de Zeeuw (Dordrecht: Reidel)
- Häußler B. et al. 2007, *ApJS*, 172, 615
- Heckman T. M., Smith E. P., Baum S. A., van Breugel W. J. M., Miley G. K., Illingworth G. D., Bothun G. D., Balick B., 1986, *ApJ*, 311, 526
- Heckman T. M., Kauffmann G., Brinchmann J., Charlot S., Tremonti C., White S., 2004, *ApJ*, 613, 109
- Hopkins P. F., Hernquist L., Cox T. J., Di Matteo T., Robertson B., Springel V., 2006, *ApJS*, 163, 1
- Hopkins P. F., Hernquist L., Cox T. J., Keres D., 2008, *ApJS*, 175, 356
- Hubble, E. P., 1936, *The Realm of the Nebulae*, New Haven, CT: Yale Univ. Press
- Hunter J. D., 2007, *Computing In Science & Engineering*, Volume 9, Issue 3, 90
- Hyvönen T., Kotilainen J. K., Örn Dahl E., Falomo R., Uslenghi M., *A & A*, 462, 525
- Inskip K. J., Tadhunter C. N., Morganti R., Holt J., Ramos-Almeida C., Dicken D., 2010, *MNRAS*, 407, 1739
- Jahnke L., Kuhlbrodt B., Wisotzki L., 2004, *MNRAS*, 352, 399
- Kauffmann G. et al., 2003, *MNRAS*, 346, 1055
- Katgert P., Katgert-Merkelin J. K., Le Poole R. S., van der Laan H., 1973, *A&A*, 23, 171
- Kim M., Ho L. C., Peng C. Y., Barth A. J., Im M., 2008, *ApJS*, 179, 283 (KIM08)
- Kim M., Ho L. C., Peng C. Y., Barth A. J., Im M., 2017, *ApJS*, 232, 2,1
- Kocevski D. D. et al. 2012, *ApJ*, 744, 148
- Kormendy J., Richstone D. 1995, *ARA&A*, 33, 581
- Kotilainen J., Falomo R., Bettoni D., Karhunen K., Uslenghi M., 2013, *Proceedings of Science*, “Nuclei of Seyfert galaxies and QSOs - Central engine & conditions of star formation”, November 6-8, 2012, MPIFR, Bonn
- Kroupa P., 2001, *MNRAS*, 322, 231
- Krist J., 1995, in *Astronomical Data Analysis Software and Systems IV*, ed. R. A. Shaw, H. E. Payne, & J. J. E. Hayes (San Francisco: ASP), 349
- Kukula M. J., Dunlop J. S., McLure R. J., Miller L., Percival W., Baum S. A., O’Dea C.P., 2001, *MNRAS*, 326, 1533
- Lackner C. N., Gunn J. E., 2012, *MNRAS*, 421, 2277
- Lacy M., 2006, in *Astrophysics Update 2*, Springer Praxis Books. ISBN 978-3-540-30312-1 [https://arxiv.org/abs/astro-ph/0601255]
- Lal V.L., Ho L.H., 2010, *AJ*, 139, 1089
- Landsman W. B., 1993 in *Astronomical Data Analysis Software and Systems II*, A.S.P. Conference Series, Vol. 52, ed. R. J. Hanisch, R. J. V. Brissenden, and Jeannette Barnes, p. 246.
- Lintott C.J. Schawinski K., Slosar A. et al., 2008, *MNRAS*, 389, 1179.
- Lucas R.A. et al. 2016, *ACS Data Handbook*, Version 8.0
- Magorrian J. et al. 1998, *AJ*, 115, 2285
- Mateos S., et al., 2017, *ApJ*, 841, L18
- Matthews T. A., Morgan W. W., Schmidt M., 1964, *ApJ*, 140, 35
- McLeod K.K., Rieke G.H., 1994, *ApJ*, 420, 58
- McLeod K.K., Rieke G.H., 1995, *ApJ*, 441, 96
- McLeod K.K., Rieke G.H., 1995, *ApJL*, 454, L77
- Nair P.B., Abraham R., 2010, *ApJSS*, 186, 427

- Peng C. Y., Ho L. C., Impey C. D., Rix H.-W., 2002, *AJ*, 124, 266
- Peng C. Y., Impey C. D., Rix H.-W., Kochanek C. S., Keeton C. R., Falco E. E., Lehár J., McLeod B. A., 2006, *ApJ*, 649, 616
- Peng C. Y., Ho L. C., Impey C. D., Rix H.-W., 2010, *AJ*, 139, 2097
- Percival W. J., Miller L., McLure R. J., Dunlop J. S., 2001, *MNRAS*, 322, 843
- Pierce C. M. et al. 2007, *ApJ*, 660, L19
- Povic M. et al. 2009, *ApJ*, 706,1
- Ramos Almeida C., Bessiere P., Tadhunter C., Pérez-González P.G., Barro G., Inskip K.J., Morganti R., Holt J., Dicken D., 2012, *MNRAS*, 419, 687.
- Reyes R. et al. 2008, *AJ*, 136, 2373
- Ribeiro B. et al., 2016, *A & A* 593, A22
- Ridgway S., Heckman T., Calzetti D., Lehnert M., 2001, *ApJ*, 550, 122
- Rodríguez Zaurín J., Tadhunter C. N., González Delgado R. M., 2010, *MNRAS*, 403, 1317
- Rodríguez Zaurín J., Arribas S., Monreal-Ibero A., Colina L., Alonso-Herrero A., Algonso-Garzón J., 2011, *A&A*, 527, A60
- Schawinski K., Treister E., Urry C. M., Cardamone C. N., Simmons B., Yi S. K., 2010, *ApJL*, 727, 2
- Smith M. G., Wright A. E., 1980, *MNRAS*, 191, 871
- Sérsic J. L., 1963, *Boletín de la Asociación Argentina de Astronomía La Plata Argentina*, 6, 41
- Shen S., Mo H. J., White S., Blanton M.R., Kauffmann G., Voges W., Brinkmann J., Csabai I., 2003, *MNRAS*, 343, 978
- Tajer M., 2007, *A&A*, 467, 73
- Taylor M. B., 2005, in Shopbell P., Britton M., Ebert R., eds, *ASP Conf. Ser. Vol. 347, Astronomical Data Analysis Software and Systems XIV*. Astron. Soc. Pac., San Francisco, p. 29
- The Astropy Collaboration: Robitaille T. P. et al, 2013. *A&A*, 558, A33
- Toomre A., Toomre J., 1972, *ApJ*, 178, 623
- Tremaine S. et al. 2002, *ApJ*, 574, 740
- Trujillo I., Aguerri J. A. L., Cepa J., Gutiérrez C. M., 2001a, *MNRAS*, 321, 269
- Uslenghi M., Falomo R., 2008, in Di Gesù V., Bosco, G.L., Maccarone, M.C., eds. *Proc. of the 6th International Workshop on Data Analysis in Astronomy, Modelling and Simulation in Science*. World Scientific, Hackensack, NJ, p. 313
- Villar Martín M., Cabrera Lavers A., Bessiere P., Tadhunter C., Rose M., de Breuck C., 2012, *MNRAS*, 423, 80
- Veilleux S., Kim D. -C., Sanders D. B., 2002, *ApJS*, 143, 315
- Weinzirl T., Jogee S., Khochfar S., Burkert A., Kormendy J., 2009, *AJ*, 696, 441
- Willett K.W., Lintott C.J., Bamford S.P. et al. 2013, *MNRAS*, 435, 2835
- Wright E.L., 2006 *PASP*, 118, 1711
- Wylezalek D., Zakamska N. L., Liu G., Obied G., 2016, *MNRAS*, 457, 745
- Zakamska N. L. et al., 2003, *AJ*, 126, 2125
- Zakamska N. L. et al., 2006, *AJ*, 132, 1496

APPENDIX A: THE POINT SPREAD FUNCTION

The final model image produced by GALFIT for a given quasar is constructed by convolving a model image of the host galaxy with a PSF. Thus, the success of the method relies on knowing an accurate PSF. This is particularly important in studies of type 1 (unobscured) AGN, where the central unresolved source can dominate entirely the flux in the central regions and the PSF wings can contaminate severely at large radii. Small variations of the PSF can lead to large variations on the inferred host galaxy properties (Kim et al. 2008, [KIM08](#) hereafter).

Although the central source in type 2 AGN is obscured and the PSF effects are less severe than in the type 1 counterparts, a good quality PSF is required. The presence of an unresolved nuclear source cannot be discarded. Scattered AGN light, nebular continuum, emission lines and nuclear star clusters may all contribute to the nuclear emission (e.g. [Balcells et al. 2007](#), [Bessiere et al. 2017](#)). The PSF profile is so steep that it can have a significant impact on the central shape and the inferred parametric properties of a galaxy even for low contributions to the total flux ($\lesssim 10\%$).

Colour, temporal and spatial variations of the PSF

The HST PSF are known to vary depending on position on the detector, time and spectral colour. Other authors (see in particular [KIM08](#)) have performed careful investigations of such dependence. Based on these works, we have assumed that the influence of the PSF colour is comparatively negligible. The ideal procedure to obtain a good quality PSF would then be to select one star or a combination of several in each AGN field close to the target ($\lesssim 100$ pixels for the WFPC2, [KIM08](#)). However, appropriate stars (i.e. not saturated and with adequate S/N to trace the core and the wings) at $\lesssim 100$ pixels are unavailable for most of the objects.

Since [KIM08](#) found that spatial variations of the PSF are significantly smaller than temporal variations, our aim has been to minimize temporal variations. The HST WFPC2 observations of our sample were concentrated around two different epochs: April to June 2007 and November 2008. The ACS observations were performed between August and December 2006.

We distributed the WFPC2 subsample in two groups (2007 and 2008) according to the two observing epochs (see [Table 1](#)). We then generated two libraries of PSF, one for each epoch. Each library contains 2D images of non-saturated stars with well detected wings selected in the images of different AGN targets. A third PSF library was built for the ACS sample.

For each epoch/instrument, we combined several stars of the field in the corresponding library normalizing the flux to unity and weighting by the S/N ratio ([Inskip et al. 2010](#)).

Undersampling of the PSF

Another aspect to take into account is that the HST PSF is undersampled in the WFPC2 images, for which the nominal FWHM is ~ 1.5 pixels. The main impact is that it is not possible to preserve the original shape of the PSF when shifting by a fraction of a pixel ([KIM08](#); [Peng et al. 2002](#)). As explained by [KIM08](#), the subpixel interpolation can change significantly both the width and the amplitude

Image	Point source			Sersic 1				Sersic 2				Class
	Total Mag (1)	Mag (2)	L.F. (%) (3)	Mag (4)	L.F. (%) (5)	r_e (6)	n (7)	Mag (8)	L.F. (%) (9)	r_e (10)	n (11)	
Galaxy 1												
a)	21.9	25.1	4.99	21.9	95.01	4.8	1.0					Disk-dominated
b)	21.9	25.1	5.64	22.0	94.36	4.6	0.8					Disk-dominated
c)	22.0	25.5	3.74	22.0	96.26	4.4	0.7					Disk-dominated
Galaxy 2												
a)	20.9			20.9	100.00	2.7	0.9					Disk-dominated
b)	20.9			20.9	100.00	2.9	1.0					Disk-dominated
c)	21.0			21.0	100.00	2.8	0.9					Disk-dominated
Galaxy 3												
a)	19.6	21.7	14.01	19.8	85.99	2.8	2.9					Bulge-dominated
b)	19.5	21.2	20.26	19.8	79.74	2.7	2.3					Bulge-dominated
c)	19.6	21.5	16.92	19.8	83.08	2.4	2.0					Bulge-dominated
Galaxy 4												
a)	20.7			22.2	25.33	1.7	1.4	21.0	74.67	6.2	0.3	Disk-dominated
b)	20.4			22.2	20.38	1.4	1.0	20.7	79.62	6.3	0.3	Disk-dominated
c)	20.4			21.9	24.93	1.5	1.7	20.7	75.07	6.4	0.2	Disk-dominated
Galaxy 5												
a)	20.9	22.5	23.8	21.2	76.16	2.1	1.9					Disk-dominated
b)	20.7	21.9	32.4	21.1	67.61	2.4	1.4					Disk-dominated
c)	20.7	21.9	33.3	21.2	66.67	2.6	1.0					Disk-dominated

Table A1. Test performed for several normal galaxies in the fields of three AGN of our WFPC2 sub-sample to investigate the impact of the PSF undersampling. The table shows the results of fitting with GALFIT the host galaxies using a) the HLA image b) the original raw unrotated image and c) this image smoothed to fulfill Nyquist sampling. Col(1): Total magnitude Mag of the GALFIT model. Cols (2) and (3) Mag and light fraction (L.F.) of the point source. Col(4) to (7) : Mag, L.F., effective radius r_e in kpc and index n of first Sérsic component. Col(8) to (11): Same for second Sérsic component. Col(12) Galaxy classification following the criteria in Sect. 3.2.4. The classification is consistent using a), b) and c) for all objects.

Image	Point source			Sersic 1				Sersic 2				Class
	Total Mag (1)	Mag (2)	L.F. (%) (3)	Mag (4)	L.F. (%) (5)	r_e (6)	n (7)	Mag (8)	L.F. (%) (9)	r_e (10)	n (11)	
SDSS J0748+39												
a)	18.7	21.3	9.45	18.6	90.55	9.4	4.3					Bulge-dominated
b)	18.6	21.3	8.63	18.5	91.37	10.1	4.5					Bulge-dominated
c)	18.7	22.2	4.14	18.5	95.86	10.9	5.3					Bulge-dominated
SDSS J0811+07												
a)	19.2			19.2	100.00	5.9	4.2					Bulge-dominated
b)	19.1			19.1	100.00	7.1	4.0					Bulge-dominated
c)	19.3			19.3	100.00	7.3	3.7					Bulge-dominated
SDSS J1726+60												
a)	19.8	20.6	47.06	20.3	52.94	2.6	1.4					Disk-dominated
b)	19.8	20.9	35.23	20.1	64.77	2.1	2.1					Bulge-dominated
c)	20.0	21.3	29.31	20.2	70.69	2.1	2.0					Bulge-dominated
SDSS J1739+54												
a)	19.2	20.9	20.51	20.3	35.8	1.9	0.8	20.1	43.72	8.5	1.0	Disk-dominated
b)	19.3	21.4	14.00	20.1	47.17	1.6	1.3	20.2	38.83	9.6	1.0	Disk-dominated
c)	19.5	23.0	3.38	20.1	55.47	1.3	1.0	20.3	41.15	8.7	0.8	Disk-dominated

Table A2. Same as Table A2 with tests performed to four AGN in the WFPC2 sample. The classification of the objects is in general consistent using a), b) and c).

of the unresolved flux, while the wings of the PSF, which are much better sampled, do not change much.

The HLA images of our sample have a FWHM \sim 2.1-2.5 pixels depending on the object, which is consistent with Nyquist-sampling. The images in the HLA are drizzled, i.e. the original pixels were mapped onto an output rotated frame, where a single pixel from the detector might be spread over more than one output pixel. This process can spread the PSF out to a larger value than the original PSF in the unrotated images.

In order to investigate the impact of an undersampled PSF, we applied a diversity of tests to 5 random normal galaxies and 4 random AGN hosts of our sample, observed in the two WFPC2 epochs and spanning morphological diversity. For these purposes, we consider “normal” galaxies, those different to the AGN targets with no obvious evidence for nuclear activity (i.e. a prominent central point source) and morphological distortions. The AGN and normal galaxies were fitted with GALFIT in 3 different images corresponding to the same field of view: a) the HLA images using combined field stars to produce the PSF (see above), b) the original, unrotated calibrated images using also combined field stars for the PSF, c) the original, unrotated calibrated images convolved with a Gaussian whose FWHM ensures achieving Nyquist-sampling (KIM08). The PSF was convolved in the exact same way.⁷

We find that a), b) and c) produce consistent results for normal (Table A1) and AGN host galaxies (Table A2) in the sense that the same number of structural components are required for a given object. The best fits are also in general consistent in terms of the r_e and n of each component. The relative contribution to the total light of a given structural component can vary up to \sim 10% at most for a given structural component for normal galaxies and up to \sim 20% for AGN hosts. The final classification of the galaxy is always consistent in a), b) and c) for normal galaxies and, in general, for AGN hosts. SDSS J1726+60 is an exception in the AGN group, although this is not surprising, since it has an intermediate n value between disk-dominated and bulge-dominated systems, so that the final classification is strongly sensitive to small n uncertainties.

Our conclusion is that the effects of undersampling for the WFPC2 do not have a significant impact on the structural parametrization of the galaxies.

APPENDIX B: BRIEF DESCRIPTION OF RELATED STUDIES

We presented in Sect. 5.1 a comparison of the results of our parametric classification with related studies. We describe here very briefly the main properties of the samples, data, methodology and classification criteria presented in these works.

- Dunlop et al. (2003) carried out a seminal work based on R band HST/WFPC2 images of the host galaxies of 13 type 1 radio-quiet (RQQ) and 10 type 1 radio-loud quasars (RLQ) at $0.11 < z < 0.26$ with nuclear absolute magnitudes

in the range $-19.7 \leq M_R \leq -25.7$. They fitted the host galaxies with one or two Sérsic components. All RLQ and 9 RQQ showed no evidence for any disk component ($n \sim 1$) and were classified as ellipticals as a result, based on the galaxy $n \gtrsim 4$ profile. Only 4 RQQ were best fitted with a combination of a disk and a bulge, two of which are dominated by the spheroid. Therefore, the analysis by Dunlop et al. (2003) results on 10/10 or 100% $_{-16}$ RLQ and 11/13 or 85% $_{-15}^{+6}$ RQQ are spheroidal or bulge-dominated. While only 15% $_{-6}^{+13}$ of RQQ are disk-dominated.

- Floyd et al. (2004) studied a sample of 17 QSO1 (10 radio-quiet and 7 radio-loud) at $0.29 < z < 0.43$, spanning a range of absolute magnitudes $-27.7 \leq M_V \leq -24.4$, using HST/WFPC2 images and the F814W or F791W filters. Accounting also for the point source central function, the authors fitted the host galaxy surface brightness profiles using a single Sérsic component. When the index is left free, they find 13/17 (76% $_{-13}^{+8}$) with $n \gtrsim 2.5$ that they classify as ellipticals (see their Table 4), 3/17 (18% $_{-7}^{+11}$) with $n = 0.75-1.04$ that they classify as disks galaxies and 1/17 (6% $_{-3}^{+11}$) is an intermediate case with $n = 1.8$.

- Falomo et al. (2014) studied the galaxy types and morphologies of 416 QSO1 at $z < 0.5$ with $M_i < -22$ using i-band SDSS images in the Stripe82 region that are significantly deeper than standard SDSS data. Most are radio-quiet. Galaxies were well resolved in 316 objects. For the classification of the host morphologies they combine the visual inspection of the images and the fits of the light profiles with a PSF and a single Sérsic component using the Astronomical Image Decomposition Analysis (AIDA; Uslenghi & Falomo 2008). They consider two types of morphology: exponential disk and de Vaucouleurs profile. They find that about 113 objects (37% $_{-3}^{+3}$) are dominated by the bulge, 129 (42% $_{-3}^{+3}$) have a conspicuous disk structure and 64 (21% $_{-3}^{+3}$) exhibit a mixed bulge plus disk structure.

- Cales et al. (2011) studied a sample of 29 post starburst QSO1 at $0.25 < z < 0.45$ with $-24.0 \leq M_r \leq -22.1$ using HST/ACS-F606W images. No information is quoted on radio-loudness. The authors classify the galaxies visually. In this way they identify an equal number of spiral (13/29, 45% $_{-10}^{+8}$) and early-type (13/29, 45% $_{-10}^{+8}$) hosts, with the remaining three hosts having indeterminate classifications (3/29, 10% $_{-4}^{+8}$). They also parametrized the galaxies with GALFIT, selecting the best fit for each object aided by the prior visual classification. They found that galaxies visually classified as early types are fitted with a single Sérsic component ($n \gtrsim 2$ in most cases) and that most galaxies visually classified as spirals or probable spirals are fitted with two Sérsic components with fixed index: $n=4$ for the bulge and $n=1$ for the disk.

Because the information in Cales et al. (2011) is not enough to identify all bulge-dominated systems, we have applied our parametric method to classify their sample (Table 7). For this, we have used the parameter values for each structural component the authors isolate in their fits. Based on their highly-disturbed morphology, we classify 4 objects as disturbed (or “Multiple Systems”). We find 13 spheroidal galaxies, 5 bulge-dominated galaxies, 3 disk-like galaxies, 3 disk-dominated galaxies and 1 object for which the bulge and the disk have similar contribution. The final classification is: 21% $_{-7}^{+8}$ disk-dominated, 62% $_{-14}^{+4}$ bulge-dominated, 3% $_{-1.2}^{+7}$ B+D galaxies and 14% $_{-5}^{+8}$ disturbed systems.

⁷ This method was also attempted using PSF created with Tiny-Tim (Krist et al. 1995), but the PSF we obtained from the data yielded better results

- [Greene et al. \(2009\)](#) studied a sample of 15 SDSS QSO2 at $0.1 < z < 0.45$ with $8.7 \lesssim IO3 \lesssim 9.3$. No information is provided on the radio-loudness, but a fraction of $\sim 15 \pm 5\%$ can be expected to be radio-loud ([Lal & Ho 2010](#)). They parametrized the host galaxies using GALFIT based on ground based r band images (except for 3 objects observed with the g and i filters). The images were obtained with the Low Dispersion Survey Spectrograph (LDSS3) at the 6.5m Clay-Magellan telescope. The authors were mostly interested on the spheroidal components. For this reason, they only introduce a disk component ($n=1$) in the galaxy model when visible in the images. In this way, they identify 4 disk galaxies (with the bulge dominating in one of them) while seven consist of a single spheroidal component. 4 highly-disturbed objects could not be fitted successfully. Therefore, the final classification is 8/15 ($53\%_{-16}^{+9}$) are bulge-dominated, 3/15 ($20\%_{-8}^{+12}$) are disk-dominated and 4/15 ($27\%_{-10}^{+12}$) are highly-disturbed systems.

- [Wylezalek et al. \(2016\)](#) analyzed HST/ACS FR914M optical images of 20 luminous ($IO3 \geq 9.0$) radio-quiet SDSS QSO2 at $0.2 < z < 0.6$. They fitted the host galaxies with GALFIT using one or two Sérsic components. For single components, they consider that a galaxy is disk-dominated when $n \leq 1$ or bulge-dominated for $n \geq 1$. When two components are isolated in the fits, they classify a galaxy as disk-dominated when the n of the brighter (or primary) component is $n_{\text{pri}} \leq 1$ and bulge-dominated when $n_{\text{pri}} \geq 1$. According to this method, they find that all but 2 QSO2 are bulge-dominated ($90\%_{-11}^{+4}$), while the remaining 2 are disk-dominated ($10\%_{-4}^{+11}$).

- [Inskip et al. \(2010\)](#) studied the parametric properties of a sample of 41 radio galaxies at $0.03 \leq z \leq 0.5$: 17 narrow line radio galaxies (NLRG), 12 broad line radio galaxies (BLRG) and 13 weak line radio galaxies (WLRG). They used ground based K-band images obtained with the instrument/telescope combinations UFTI/UKIRT, ISAAC/VLT and, most them, with SOFI/NTT. Here we compare with the NLRG sample: although powerful radio sources, if they were classified based only on their optical emission line spectroscopic properties ([Zakamska et al. 2003](#)) they would be classified as QSO2.

The authors used GALFIT for their analysis in 16 NLRG (one of them was too faint to model). They fit most host galaxies with a single Sérsic component, including also a point source in a significant fraction of objects (see Sect. 4.4). In general, most galaxies (14/16 or $88\%_{-17}^{+1}$) are fitted with a $n=4$ or $n=6$ Sérsic, which they classify as “bulges”. 1/16 or $6\%_{-3}^{+11}$ is fitted with a $n=2$ Sérsic, which they classify as “disk”. Finally, 1/16 or $6\%_{-3}^{+11}$ consists of a disk and bulge, which they classify as “mixed”.